

# Mesenchymal stem cell transplantation in tight-skin mice identifies miR-151-5p as a therapeutic target for systemic sclerosis

Chider Chen<sup>1</sup>, Dandan Wang<sup>2</sup>, Alireza Moshaverinia<sup>3</sup>, Dawei Liu<sup>1</sup>, Xiaoxing Kou<sup>1</sup>, Wenjing Yu<sup>1</sup>, Ruili Yang<sup>1</sup>, Lingyun Sun<sup>2</sup>, Songtao Shi<sup>1</sup>

<sup>1</sup>Department of Anatomy and Cell Biology, University of Pennsylvania, School of Dental Medicine, Philadelphia, PA 19104, USA;

<sup>2</sup>Department of Rheumatology and Immunology, The Affiliated Drum Tower Hospital of Nanjing University Medical School, 321 Zhongshan Road, Nanjing, Jiangsu 210008, China; <sup>3</sup>Division of Advanced Prosthodontics, Weintraub Center for Reconstructive Biotechnology, School of Dentistry, University of California, Los Angeles, CA 90095, USA

**Systemic sclerosis (SSc), an autoimmune disease, may cause significant osteopenia due to activation of the IL4R $\alpha$ /mTOR pathway. Mesenchymal stem cell transplantation (MSCT) can ameliorate immune disorders in SSc via inducing immune tolerance. However, it is unknown whether MSCT rescues osteopenia phenotype in SSc. Here we show that MSCT can effectively ameliorate osteopenia in SSc mice by rescuing impaired lineage differentiation of the recipient bone marrow MSCs. Mechanistically, we show that donor MSCs transfer miR-151-5p to the recipient bone marrow MSCs in SSc mice to inhibit IL4R $\alpha$  expression, thus downregulating mTOR pathway activation to enhance osteogenic differentiation and reduce adipogenic differentiation. Moreover, systemic delivery of miR-151-5p is capable of rescuing osteopenia, impaired bone marrow MSCs, tight skin, and immune disorders in SSc mice, suggesting that miR-151-5p may be a specific target for SSc treatment. Our finding identifies a previously unrecognized role of MSCT in transferring miRNAs to recipient stem cells to ameliorate osteopenia via rescuing a non-coding RNA pathway.**

**Keywords:** mesenchymal stem cell; systemic sclerosis; osteopenia; microRNA-151-5p; exosome

*Cell Research* (2017) 27:559–577. doi:10.1038/cr.2017.11; published online publication 20 January 2017

## Introduction

Systemic sclerosis/scleroderma (SSc) is a connective tissue disorder characterized by progressive fibrosis of the skin, internal organ dysfunction, vasculopathy, and autoimmune rheumatic conditions [1]. Osteopenia of the vertebrae and other bones are commonly observed in SSc patients [2–6]. It has been suggested that bone loss in SSc patients may be due to immobilization, and medical treatments such as use of corticosteroids [7]. However, the detailed pathophysiological mechanism of bone de-

fects in SSc patients is largely unknown.

Fibrillin-1 (Fbn1)-mutant tight-skin mice (B6.Cg-Fbn1<sup>Tsk/J</sup>; *Tsk*<sup>+</sup>), an established SSc model, show significantly reduced femoral bone mineral density (BMD) and abnormal trabecular bone microarchitecture [8]. Recent studies indicate that type 2 helper T-cell (T<sub>H</sub>2) infiltration and interleukin-4 (IL4), a key T<sub>H</sub>2 cytokine, play a critical role in the regulation of fibrotic tissue deposition and bone marrow mesenchymal stem cells (BMMSCs) [9]. Downregulation of the IL4/IL4R $\alpha$  signaling pathway in *Tsk*<sup>+</sup> mice can rescue fibrotic and osteoporotic phenotypes, suggesting that IL4 signaling contributes to the pathological process in SSc [10, 11].

Systemic MSC transplantation (MSCT) has been used to treat a variety of human diseases such as graft versus host disease (GvHD), systemic lupus erythematosus (SLE), diabetes, rheumatoid arthritis, myocardial infarction, liver fibrosis, inflammatory bowel disease,

Correspondence: Songtao Shi<sup>a</sup>, Lingyun Sun<sup>b</sup>

<sup>a</sup>Tel: 215-898-3326; Fax: 215-573-5032

E-mail: songtaos@dental.upenn.edu

<sup>b</sup>E-mail: lingyunsun2012@163.com

Received 11 May 2016; revised 3 October 2016; accepted 6 December 2016; published online publication 20 January 2017

autoimmune encephalomyelitis, periodontitis, sepsis and scleroderma [12–23]. At the molecular level, MSCT may employ a paracrine cytokine secretion mechanism to regulate recipient immune response, thereby achieving therapeutic effects [24–27]. In addition, MSCT is able to induce immune tolerance and ameliorate autoimmune phenotypes in SSc through activation of the Fas/Fas ligand pathway, leading to apoptosis of activated T cells [28, 29]. However, it is unknown whether MSCT ameliorates the osteoporotic phenotype and rescues impaired BMMSCs in SSc.

MicroRNAs (miRNAs) are small non-coding RNAs that function as post-transcriptional regulators of gene expression [30]. It has been shown that coding and non-coding RNAs can be transferred between cells by small vesicles called exosomes [31–33]. Releasing large amounts of exosomes is one mean by which MSCs communicate with surrounding cells, implying that exosome-mediated cellular content transfer may serve as a novel mechanism offering therapeutic effects in MSCT [34, 35]. In this study, we show that MSCT transfers miR-151-5p to *Tsk*<sup>+/+</sup> recipients, rescuing impaired lineage differentiation of BMMSCs and osteopenia *via* regulating the IL4R $\alpha$ /mTOR pathway.

## Results

### *MSCT rescues osteopenia in Tsk<sup>+/+</sup> mice by regulating osteo/adipo-genic lineage differentiation of recipient BMMSCs*

*Tsk*<sup>+/+</sup> SSc mice exhibit significantly reduced bone volume and increase of bone marrow adipocytes [8, 11]. Since MSCT is able to ameliorate the osteoporotic phenotypes observed in SLE and ovariectomized (OVX) mice [13, 36, 37], we hypothesized that this therapeutic effect could extend to SSc. We therefore used allogeneic MSCT to treat *Tsk*<sup>+/+</sup> mice at 8 weeks of age and examined the therapeutic effects at 16 weeks of age (Figure 1A). MicroCT and histological analysis confirmed that BMD and distal femoral trabecular bone volume of *Tsk*<sup>+/+</sup> mice were markedly decreased compared with the control wild-type (WT) littermates (Figure 1B–1D). BMMSC transplantation (MSCT) significantly rescued BMD and trabecular bone volume in *Tsk*<sup>+/+</sup> mice (Figure 1B–1D). A histomorphometric analysis indicated that osteoblast and osteoclast numbers in the femurs of *Tsk*<sup>+/+</sup> mice using alkaline phosphatase (ALP) immunohistochemical and tartrate-resistant acid phosphatase (TRAP) staining, respectively, were significantly reduced when compared to the control littermates (Figure 1E and 1F). MSCT significantly restored osteoblast and osteoclast numbers in the femurs of *Tsk*<sup>+/+</sup> mice (Figure 1E and 1F). In addition, serum levels of soluble receptor activator of nuclear factor

$\kappa$ B ligand (sRANKL) and type I collagen cross-linked telopeptide (CTX) were significantly reduced in *Tsk*<sup>+/+</sup> mice (Figure 1G and 1H). MSCT markedly improved the serum levels of CTX and sRANKL (Figure 1G and 1H), suggesting that bone volume loss is mainly caused by insufficient osteoblast function in *Tsk*<sup>+/+</sup> mice. To further confirm this observation, we performed a calcein-labeling assay to show that bone turnover rate was decreased in *Tsk*<sup>+/+</sup> mice, whereas MSCT significantly improved bone formation rate (Figure 1I).

To examine whether MSCT rescued BMMSC lineage differentiation in *Tsk*<sup>+/+</sup> mice, we isolated BMMSCs from MSCT-treated and untreated *Tsk*<sup>+/+</sup> mice. Our analysis revealed that the number of colony forming unit-fibroblasts (CFU-F) was significantly reduced in *Tsk*<sup>+/+</sup> mice compared to the control group, while MSCT significantly elevated the numbers of CFU-F (Figure 2A). When cultured under osteogenic induction conditions, *Tsk*<sup>+/+</sup> BMMSCs showed impaired osteogenic differentiation, as indicated by reduced mineralized nodule formation (assessed by alizarin red staining) and reduced expression of the osteogenic genes runt-related transcription factor 2 (*Runx2*), *ALP*, and osteocalcin (*OCN*) (Figure 2B and 2C). MSCT was able to rescue impaired osteogenic differentiation of BMMSCs from *Tsk*<sup>+/+</sup> mice, as observed by increased mineralized nodule formation and expression of *Runx2*, *ALP*, and *OCN* (Figure 2B and 2C). We next showed that BMMSCs derived from *Tsk*<sup>+/+</sup> mice generated less new bone than BMMSCs from the control group at 8 weeks post implantation using an established *in vivo* BMMSC implantation assay, in which  $4 \times 10^6$  BMMSCs with hydroxyapatite tricalcium phosphate (HA/TCP) particles as a carrier were subcutaneously implanted into immunocompromised mice (Figure 2D). The impaired *Tsk*<sup>+/+</sup> BMMSCs were rescued by MSCT as indicated by increased *in vivo* bone formation (Figure 2D). In addition to impaired osteogenesis, *Tsk*<sup>+/+</sup> mice showed a markedly increased number of adipocytes in the bone marrow (Figure 2E). MSCT largely diminished numbers of adipocytes in the bone marrow of *Tsk*<sup>+/+</sup> mice (Figure 2E). When cultured under adipogenic induction conditions, *Tsk*<sup>+/+</sup> BMMSCs showed increased numbers of Oil red O-positive cells and upregulation of adipogenic genes peroxisome proliferator-activated receptor gamma 2 (*PPAR $\gamma$* ) and lipoprotein lipase (*LPL*); MSCT significantly reduced the number of Oil red O-positive cells and expression levels of *PPAR $\gamma$*  and *LPL* in *Tsk*<sup>+/+</sup> BMMSCs (Figure 2F and 2G). Based on these results, we conclude that the osteopenia in *Tsk*<sup>+/+</sup> mice is associated with altered lineage differentiation of BMMSCs, resulting in a decreased rate of bone formation. MSCT successfully ameliorates osteopenia in SSc mice *via* res-

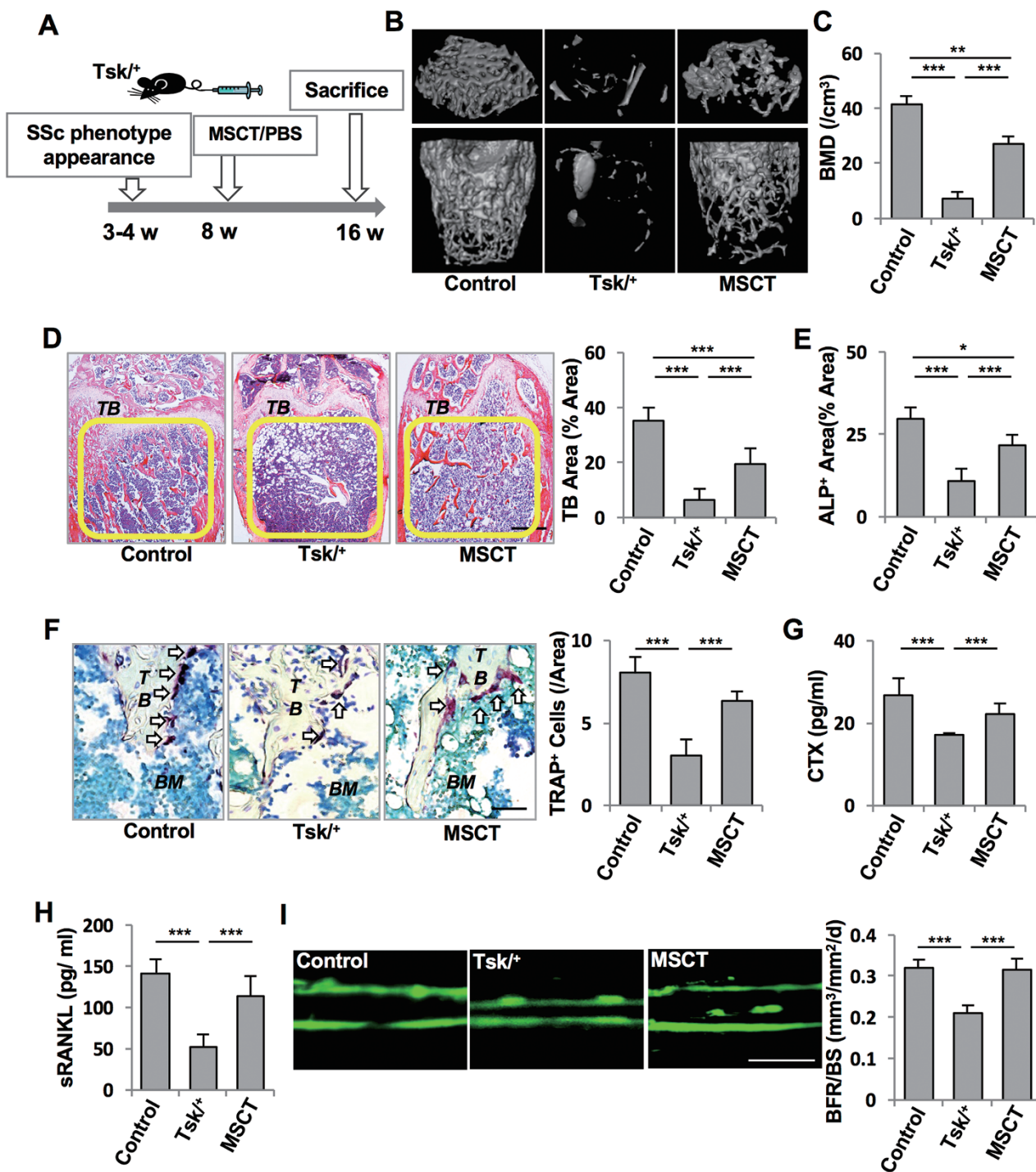


**Figure 1** MSCT rescued osteopenia in *Tsk*<sup>+/+</sup> mice. **(A)** Experimental outline describing the use of MSCT to treat *Tsk*<sup>+/+</sup> mice ( $n = 6$  per group). **(B, C)** MicroCT analysis showing images **(B)** and bone mineral density (BMD) **(C)** of trabecular bone (TB) area in distal femurs of wild-type (WT) control, *Tsk*<sup>+/+</sup>, and MSCT-treated *Tsk*<sup>+/+</sup> mice. **(D)** H&E staining showing TB volume (yellow-circled area) in WT, *Tsk*<sup>+/+</sup>, and MSCT-treated *Tsk*<sup>+/+</sup> mouse distal femurs, Scale bar, 1 mm. **(E)** Immunohistochemical staining of ALP<sup>+</sup> osteoblasts in WT, *Tsk*<sup>+/+</sup>, and MSCT-treated mice. **(F)** TRAP staining of osteoclasts in distal femur TB and bone marrow (BM) in WT, *Tsk*<sup>+/+</sup>, and MSCT-treated *Tsk*<sup>+/+</sup> mice. Arrowheads, TRAP<sup>+</sup> osteoclasts (purple cells). Scale bar, 25  $\mu\text{m}$ . **(G, H)** ELISA analysis showing the levels of serum CTX **(G)** and sRANKL **(H)** in WT, *Tsk*<sup>+/+</sup>, and MSCT-treated *Tsk*<sup>+/+</sup> mice. **(I)** Calcein double labeling of the metaphyseal TB in the distal femurs showing the bone turnover rate in WT, *Tsk*<sup>+/+</sup>, and MSCT-treated *Tsk*<sup>+/+</sup> mice. Scale bar, 25  $\mu\text{m}$ . All experimental data were verified in at least three independent experiments. Error bars represent the s.d. from the mean values. \*\*\**P* < 0.005; \*\**P* < 0.01; \**P* < 0.05.

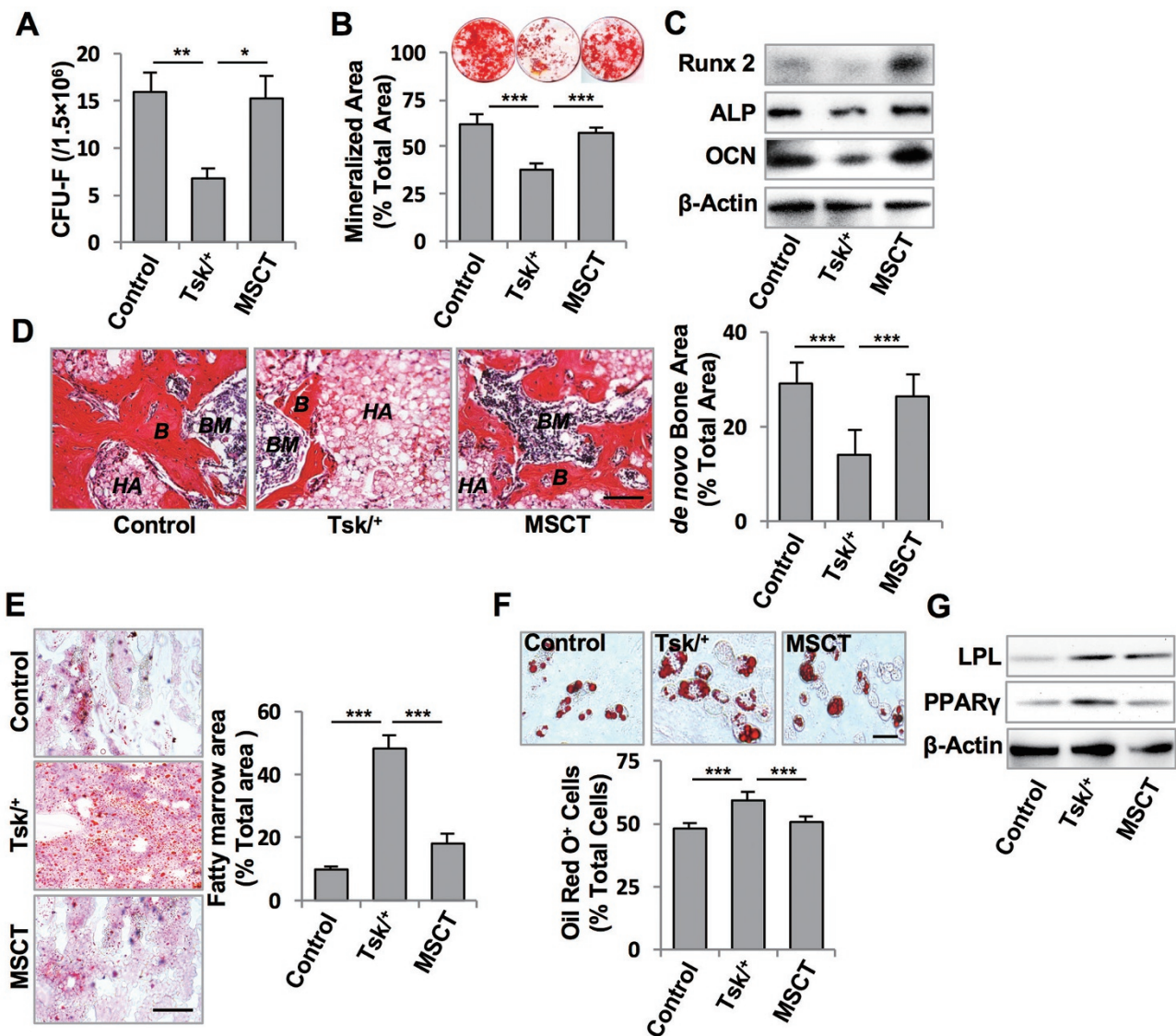


**Figure 2** MSCT rescued impaired lineage differentiation of BMMSCs in *Tsk1<sup>+</sup>* mice. **(A)** Toluidine blue staining showing the number of CFU-F from WT control, *Tsk1<sup>+</sup>*, and MSCT-treated *Tsk1<sup>+</sup>* BMMSCs. **(B)** Alizarin red staining of WT, *Tsk1<sup>+</sup>*, and MSCT-treated *Tsk1<sup>+</sup>* BMMSCs showing the capacity to form mineralized nodules when cultured under the osteoinductive conditions. **(C)** Western blotting analysis of WT, *Tsk1<sup>+</sup>*, and MSCT-treated *Tsk1<sup>+</sup>* BMMSCs showing the expression levels of the osteogenic genes *Runx2*, *ALP*, and *OCN*.  $\beta$ -Actin was used as a protein loading control. **(D)** Subcutaneous implantation of WT, *Tsk1<sup>+</sup>*, and MSCT-treated *Tsk1<sup>+</sup>* BMMSCs in immunocompromised mice showing that new bone (B) and connective tissue (CT) were generated around the HA/TCP (HA) carrier at 8 weeks post implantation. Scale bar, 50  $\mu$ m. A semiquantitative analysis shows the amount of bone formation in BMMSC implants. **(E)** Histological images of distal femurs showing the number of adipocytes in WT, *Tsk1<sup>+</sup>*, and MSCT-treated *Tsk1<sup>+</sup>* mouse bone marrow, as assessed by Oil red O staining. Scale bar, 50  $\mu$ m. **(F)** The number of Oil red O<sup>+</sup> cells in WT, *Tsk1<sup>+</sup>*, and MSCT-treated *Tsk1<sup>+</sup>* BMMSCs under the adipogenic conditions. **(G)** The expression levels of adipogenic genes *PPAR $\gamma$*  and *LPL* in WT, *Tsk1<sup>+</sup>*, and MSCT-treated *Tsk1<sup>+</sup>* BMMSCs under the adipogenic conditions. All experimental data were verified in at least three independent experiments. Error bars represent the s.d. from the mean values. \*\*\* $P < 0.005$ ; \*\* $P < 0.001$ ; \* $P < 0.05$ .

cluding BMMSC lineage differentiation.

*MSCT transfers miR-151-5p to Tsk1<sup>+</sup>-recipient BMMSCs to rescue impaired osteo-/adipo-lineage differentiation*

Since T<sub>H</sub>2 cell infiltration and activation of IL4 signaling may contribute to SSc disease phenotypes [9-11], we examined whether MSCT regulates IL4 downstream signaling in *Tsk1<sup>+</sup>* BMMSCs. Western blot analysis

showed upregulation of IL4 signaling downstream molecules such as phosphoinositide 3-kinase (PI3K)-p110, phosphorylated Akt (p-Akt), and phosphorylated mTOR (p-mTOR) in *Tskl*<sup>+</sup> BMMSCs, whereas MSCT markedly

downregulated the levels of PI3K, p-Akt, and p-mTOR (Figure 3A). Interestingly, the expression level of IL-4R $\alpha$  was also rescued by MSCT, as shown by western blotting and quantitative PCR (qPCR) experiments

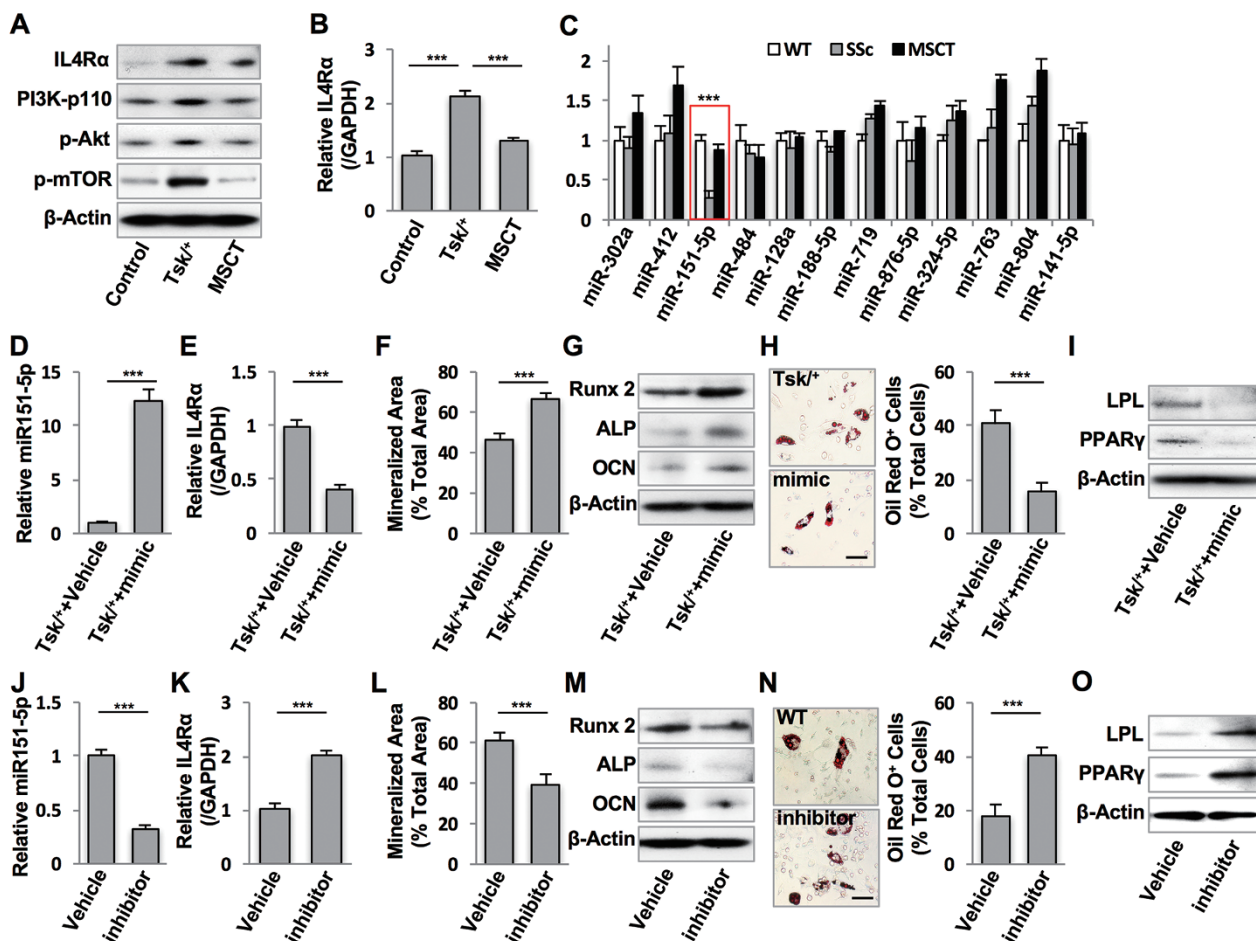


**Figure 3** MSCT transferred miR-151-5p into *Tskl*<sup>+</sup> BMMSCs to regulate IL4R $\alpha$ /mTOR signaling. **(A)** Western blot showing the expression levels of mTOR signaling genes, including IL4R $\alpha$ , PI3K-p110, p-Akt, and p-mTOR in WT, *Tskl*<sup>+</sup>, and MSCT-treated *Tskl*<sup>+</sup> BMMSCs. **(B)** qPCR analysis showing the expression levels of *Il4ra* in WT, *Tskl*<sup>+</sup>, and MSCT-treated *Tskl*<sup>+</sup> BMMSCs. **(C)** qPCR analysis showing the levels of miRNAs in WT, *Tskl*<sup>+</sup>, and MSCT-treated *Tskl*<sup>+</sup> BMMSCs. **(D)** qPCR analysis showing the levels of miR-151-5p in vehicle and miR-151-5p mimic-treated *Tskl*<sup>+</sup> BMMSCs. **(E)** qPCR analysis showing the expression levels of *Il4ra* in vehicle and miR-151-5p mimic-treated *Tskl*<sup>+</sup> BMMSCs. **(F)** Alizarin red staining showing that vehicle and miR-151-5p mimic-treated *Tskl*<sup>+</sup> BMMSCs form mineralized nodules when cultured under osteoinductive conditions. **(G)** Western blotting analysis showing the expression levels of the osteogenic genes *Runx2*, *ALP*, and *OCN* in vehicle- and miR-151-5p mimic-treated *Tskl*<sup>+</sup> BMMSCs.  $\beta$ -Actin was used as a protein loading control. **(H)** The number of Oil red O<sup>+</sup> cells in vehicle- and miR-151-5p mimic-treated *Tskl*<sup>+</sup> BMMSCs under the adipogenic conditions. **(I)** Western blotting showing the expression levels of the adipogenic genes *PPAR $\gamma$*  and *LPL* in vehicle- and miR-151-5p mimic-treated *Tskl*<sup>+</sup> BMMSCs when cultured under adipogenic conditions. **(J)** qPCR analysis showing the levels of miR-151-5p in vehicle- and miR-151-5p inhibitor-treated WT BMMSCs. **(K)** qPCR analysis showing the expression levels of *Il4ra* in vehicle- and miR-151-5p inhibitor-treated WT BMMSCs. **(L)** Alizarin red staining showing that vehicle- and miR-151-5p inhibitor-treated WT BMMSCs form mineralized nodules under osteoinductive conditions. **(M)** Western blotting showing the expression levels of the osteogenic genes *Runx2*, *ALP*, and *OCN* in vehicle- and miR-151-5p inhibitor-treated WT BMMSCs.  $\beta$ -Actin was used as a protein loading control. **(N)** The number of Oil red O<sup>+</sup> cells in vehicle- and miR-151-5p inhibitor-treated WT BMMSCs under adipogenic conditions. **(O)** Western blotting showing the expression levels of the adipogenic genes *PPAR $\gamma$*  and *LPL* in vehicle- and miR-151-5p inhibitor-treated WT BMMSCs when cultured under adipogenic conditions. All experimental data were verified in at least three independent experiments. Error bars represent the s.d. from the mean values. \*\*\**P* < 0.005.

(Figure 3A and 3B). This finding prompted us to further examine how MSCT regulates IL4R $\alpha$  expression in *Tsk*<sup>+</sup> BMMSCs. As MSCs are able to transfer miRNAs to surrounding cells in cancer and other disease models [38-40], here we asked whether miRNAs, which are small non-coding RNAs (~22 nucleotides) capable of silencing gene expression at post-transcriptional level [41], are involved in MSCT-mediated regulation of IL4R $\alpha$  expression. We used a software available online, MicroCosm Targets, to computationally identify 19 miRNAs that may target *Il4ra* gene expression (Supplementary information, Table S1). Although the levels of several miRNAs were increased after MSCT treatment in SS mice, qPCR analysis showed that only miR151-5p was significantly decreased in *Tsk*<sup>+</sup> BMMSCs (Figure 3C). After MSCT treatment, the level of miR-151-5p was significantly increased in *Tsk*<sup>+</sup> BMMSCs, suggesting that IL4R $\alpha$  expression may be regulated by miR-151-5p (Figure 3C). To further confirm the functional role of miR-151-5p, we used different amounts of miR151-5p mimic and inhibitor to treat BMMSCs and found that 25 pmol miR151-5p mimic and inhibitor provided optimal effects on regulating IL4R $\alpha$  expression in BMMSCs (Supplementary information, Figure S1). We treated *Tsk*<sup>+</sup> BMMSCs with a miR-151-5p mimic to increase the levels of miR-151-5p and found that *Il4ra* expression was significantly decreased (Figure 3D and 3E). Moreover, miR-151-5p mimic improved osteogenic differentiation of *Tsk*<sup>+</sup> BMMSCs, as indicated by alizarin red staining to show increased mineralized nodule formation and western blotting to show elevated expression of *Runx2*, *ALP*, and *OCN* (Figure 3F and 3G). Conversely, miR-151-5p mimic inhibited adipogenic differentiation in *Tsk*<sup>+</sup> BMMSCs, as indicated by a decreased number of Oil red O-positive cells and downregulation of *PPAR $\gamma$*  and *LPL* (Figure 3H and 3I). In contrast, miR-151-5p inhibitor treatment reduced the levels of miR-151-5p, elevated the expression levels of *Il4ra* in WT BMMSCs (Figure 3J and 3K), and impaired osteogenic differentiation, as indicated by reduced mineralized nodule formation (Figure 3L), downregulation of *Runx2*, *ALP*, and *OCN* (Figure 3M), an elevated number of Oil red O-positive cells (Figure 3N), and upregulation of the adipogenic genes *PPAR $\gamma$*  and *LPL* (Figure 3O).

As miR-151-5p is 100% identical in mice and humans (Supplementary information, Figure S2A), we reasoned that human miR-151-5p may also target human *Il4ra*, as predicted by microRNA.org (Supplementary information, Figure S2B). We further confirmed that miR-151-5p inhibitor treatment significantly reduced the levels of miR-151-5p (Supplementary information, Figure S3A), upregulated *hIl4ra* expression (Supplementary informa-

tion, Figure S3B), decreased osteogenic differentiation as indicated by reduced mineralized nodule formation (Supplementary information, Figure S3C), downregulated expression of *Runx2*, *ALP*, and *OCN* (Supplementary information, Figure S3D), elevated the number of Oil red O-positive cells (Supplementary information, Figure S3E), and upregulated expression of the adipogenic genes *PPAR $\gamma$*  and *LPL* (Supplementary information, Figure S3F) in human BMMSCs. To confirm that IL4 can induce downstream mTOR signaling in human BMMSCs, we showed that recombinant IL4 treatment resulted in upregulation of p-mTOR with downregulation of *Runx2*, *ALP*, and *OCN* and decreased *in vitro* mineralized nodule formation (Supplementary information, Figure S4A and S4B). Treatment with rapamycin, an mTOR signaling specific inhibitor, rescued the IL4-induced osteogenic differentiation deficiency (Supplementary information, Figure S4A and S4B). Next, we used miR-151-5p mimic to treat IL4-induced human BMMSCs and found increased levels of miR-151-5p and reduced expression levels of *Il4ra* (Supplementary information, Figure S4C and S4D). In addition, we showed that osteogenic differentiation of IL4-induced human BMMSCs was significantly improved after miR-151-5p mimic treatment, as indicated by alizarin red staining to show increased mineralized nodule formation and western blotting to show elevated expression of *Runx2*, *ALP*, and *OCN* (Supplementary information, Figure S4E and S4F). Conversely, the elevated adipogenic differentiation in IL4-induced human BMMSCs was significantly reduced in the miR151-5p mimic treatment group, as indicated by a decreased number of Oil red O-positive cells and downregulation of *PPAR $\gamma$*  and *LPL* (Supplementary information, Figure S4G and S4H). Collectively, these data suggest that MSCT transferred miR-151-5p to *Tsk*<sup>+</sup>-recipient BMMSCs to block the IL4R $\alpha$  pathway and rescue impaired lineage differentiation of recipient cells.

#### *MSCT employs extracellular vesicles to rescue Tsk<sup>+</sup> BMMSCs*

To determine how MSCT transfers miR-151-5p to recipient cells, we co-cultured WT BMMSCs with *Tsk*<sup>+</sup> BMMSCs in a transwell system to examine whether miR-151-5p can be transferred *in vitro*. After 3 days of co-culture, we observed elevated intracellular levels of miR-151-5p, decreased *Il4ra* gene expression, and improved osteogenic differentiation in *Tsk*<sup>+</sup> BMMSCs, as assessed by qPCR, alizarin red staining, and western blotting experiments, respectively (Figure 4A-4C). These data suggest that WT BMMSCs may release miR-151-5p to regulate *Tsk*<sup>+</sup> BMMSCs. As EVs, which include exosomes [42], have been shown to carry RNAs for intercellular crosstalk [31-33], we next examined whether

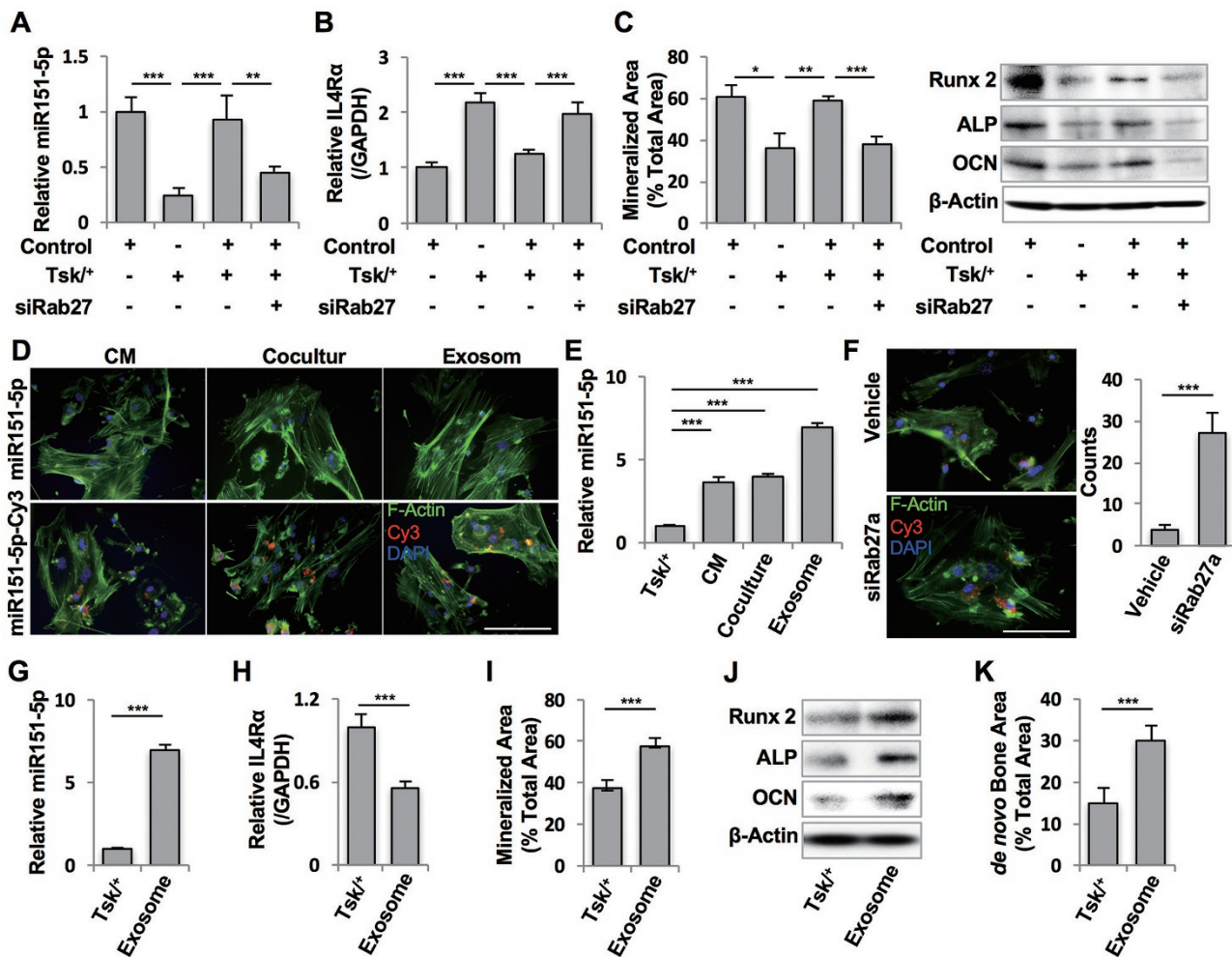


**Figure 4** Exosome-mediated miR-151-5p transfer rescued impaired *Tsk<sup>+/+</sup>* BMMSCs. **(A)** When *Tsk<sup>+/+</sup>* BMMSCs were cocultured with WT BMMSCs using a transwell system, qPCR analysis showed that intracellular levels of miR-151-5p in *Tsk<sup>+/+</sup>* BMMSCs were elevated. Blockage of exosome release from WT BMMSCs by *rab27a* siRNA attenuated intracellular miR-151-5p levels in *Tsk<sup>+/+</sup>* BMMSCs. **(B)** qPCR analysis showing the expression levels of *Il4ra* in WT, *Tsk<sup>+/+</sup>*, cocultured *Tsk<sup>+/+</sup>* with WT, and cocultured *Tsk<sup>+/+</sup>* with *rab27a* siRNA-treated WT BMMSCs. **(C)** Alizarin red staining showing the capacity to form mineralized nodules and western blotting showing the expression levels of osteogenic genes *Runx2*, *ALP*, and *OCN* in WT, *Tsk<sup>+/+</sup>*, cocultured *Tsk<sup>+/+</sup>* with WT, and cocultured *Tsk<sup>+/+</sup>* with *rab27a* siRNA-treated WT BMMSCs under osteoinductive conditions.  $\beta$ -Actin was used as a protein loading control. **(D)** Left panel: after miR-151-5p-Cy3 was transfected into WT BMMSCs, conditioned medium (CM) was harvested and loaded onto *Tsk<sup>+/+</sup>* BMMSCs to show that miR-151-5p-Cy3 was able to transfer to *Tsk<sup>+/+</sup>* BMMSCs. Middle panel: using a transwell co-culture system, miR-151-5p-Cy3-transfected WT BMMSCs were co-cultured with *Tsk<sup>+/+</sup>* BMMSCs to show that miR-151-5p-Cy3 was able to be transferred from WT to *Tsk<sup>+/+</sup>* BMMSCs. Right panel: after miR-151-5p-Cy3 was transfected into WT BMMSCs, exosomes were isolated and loaded onto *Tsk<sup>+/+</sup>* BMMSCs to show that miR-151-5p-Cy3 was able to transfer via exosomes to *Tsk<sup>+/+</sup>* BMMSCs. Scale bar, 25  $\mu$ m. **(E)** After miR-151-5p-Cy3 transfection in WT BMMSCs, miR-151-5p intracellular levels were examined by performing qPCR analysis of transfected CM-treated *Tsk<sup>+/+</sup>*, cocultured transfected BMMSCs with *Tsk<sup>+/+</sup>*, and exosome-treated *Tsk<sup>+/+</sup>* BMMSCs. **(F)** To examine the role of Rab27a in exosome-mediated miR-151-5p transfer, *Rab27a* siRNA was co-transfected with miR151-5p-Cy3 into WT BMMSCs to show that miR-151-5p-Cy3 accumulated in the transfected BMMSCs compared to the scrambled siRNA transfected group, indicating that exosome-mediated miR-151-5p transfer was blocked by Rab27a. Scale bar, 25  $\mu$ m. **(G-K)** After exosomes derived from WT BMMSCs were used to treat *Tsk<sup>+/+</sup>* BMMSCs, qPCR analysis showed elevated intracellular levels of miR-151-5p **(G)** and reduced expression levels of *Il4ra* **(H)**, along with elevated mineralized nodule formation, as assessed by alizarin red staining **(I)**, and increased expression of the osteogenic genes *Runx2*, *ALP*, and *OCN*, assessed by western blotting **(J)**. When implanted into immunocompromised mice subcutaneously, increased new bone formation was observed **(K)**. All experimental data were verified in at least three independent experiments. Error bars represent the s.d. from the mean values. \*\*\* $P < 0.005$ ; \*\* $P < 0.001$ ; \* $P < 0.05$ .

the secretion of EVs by BMMSCs can rescue impaired *Tsk*<sup>+/+</sup> BMMSCs. Using an siRNA approach to knock-down *rab27a* expression (Supplementary information, Figure S5A) to block extracellular vesicle (EV)/exosome secretion [43], we found that *rab27a* knockdown attenuated WT BMMSC-mediated rescue of intracellular miR-151-5p levels and *Il4ra* expression, as well as osteogenic differentiation in *Tsk*<sup>+/+</sup> BMMSCs (Figure 4A-4C). Next, we confirmed that purified EVs/exosomes from BMMSCs expressed exosome-specific markers CD63 and CD81 by western blotting (Supplementary information, Figure S5B) and then we labeled miR-151-5p with Cy3 red fluorescent dye to show its co-localization with the exosome marker CD63 in BMMSCs (Supplementary information, Figure S5C). In order to examine whether miR-151-5p can transfer between cultured BMMSCs, we co-cultured *Tsk*<sup>+/+</sup> BMMSCs with miR151-5p-cy3-transfected WT BMMSCs, conditioned medium from transfected BMMSCs, and EVs/exosomes from transfected BMMSCs. We showed that miR-151-5p can be transferred through EVs to *Tsk*<sup>+/+</sup> BMMSCs (Figure 4D) along with elevated levels of intracellular miR151-5p (Figure 4E). To further confirm EV/exosome-mediated miR-151-5p transfer, we used *rab27a* siRNA to block EV/exosome release in WT BMMSCs and found that miR151-5p transfer was markedly inhibited (Figure 4F). When EVs from WT BMMSCs were added to cultured *Tsk*<sup>+/+</sup> BMMSCs, the levels of intracellular miR-151-5p were increased, and the expression levels of *Il4ra* were decreased (Figure 4G and 4H). In addition, the EV treatment was able to improve osteogenic differentiation of *Tsk*<sup>+/+</sup> BMMSCs, as assessed by increased mineralized nodule formation, upregulation of the *Runx2*, *ALP*, and *OCN*, and increased *in vivo* bone formation (Figure 4I-4K). To address whether MSCT releases EVs/exosomes in *Tsk*<sup>+/+</sup> mice, we transfected the CD63-GFP reporter vector into BMMSCs and performed MSCT in *Tsk*<sup>+/+</sup> mice. After MSCT, immunofluorescence (IF) staining showed that CD63 co-localized with the BMMSC marker CD105 in both the femur and skin in *Tsk*<sup>+/+</sup> mice (Supplementary information, Figure S5D). We next labeled BMMSCs with red fluorescent dye, followed by transfection of the CD63-GFP reporter vector and performed MSCT in *Tsk*<sup>+/+</sup> mice to show that transplanted BMMSCs were not engrafted into the femur or skin in *Tsk*<sup>+/+</sup> mice (Supplementary information, Figure S5E). To assess whether EVs/exosomes transfer miR151-5p *in vivo*, we co-transfected the CD63-GFP reporter vector with Cy3-labeled miR151-5p into BMMSCs and performed MSCT in *Tsk*<sup>+/+</sup> mice. The data showed that MSCT-released CD63-GFP<sup>+</sup> EVs were co-localized with Cy3-miR151-5p, indicating that MSCT was associated with the secretion of exosomal

miR151-5p in *Tsk*<sup>+/+</sup> mice (Supplementary information, Figure S5F). Taken together, these experimental data indicate that MSCT-released EVs transferred miR151-5p to *Tsk*<sup>+/+</sup> BMMSCs to rescue the disease phenotypes.

We next infused EVs into *Tsk*<sup>+/+</sup> mice to observe their *in vivo* therapeutic effects. After intravenous infusion into *Tsk*<sup>+/+</sup> mice, contents of EVs were detected in bone marrow cells at 24 h post transplantation (Supplementary information, Figure S5G) and *Tsk*<sup>+/+</sup> BMMSCs showed elevated intracellular levels of miR-151-5p (Figure 5A) and reduced expression levels of *Il4ra* (Figure 5B). To further confirm that the increased miR151-5p was mainly transferred by EVs, we used miR151-5p inhibitor to generate miR-151-5p-depleted EVs and infused them into *Tsk*<sup>+/+</sup> mice, and found that miR-151-5p-depleted EVs failed to elevate intracellular levels of miR-151-5p (Figure 5A) and reduce expression levels of *Il4ra* (Figure 5B). Increased osteogenic differentiation was also observed upon infusion of EVs, as assessed by alizarin red staining to show elevated mineralized nodule formation (Figure 5C), western blotting to show upregulation of the osteogenic genes *Runx2*, *ALP*, and *OCN* (Figure 5D), and *in vivo* implantation to show elevated bone formation capacity (Figure 5E), while miR-151-5p-depleted EVs failed to increase osteogenic differentiation (Figure 5C-5E). In contrast, BMMSCs from EV-treated, but not miR-151-5p-depleted EV-treated *Tsk*<sup>+/+</sup> mice, showed a significant reduction in adipogenic differentiation, as shown by decreased numbers of Oil red O-positive cells and downregulation of the adipogenic genes *PPAR $\gamma$*  and *LPL* (Figure 5F and 5G). MicroCT and histological analysis showed that EV-treated *Tsk*<sup>+/+</sup> mice have significantly increased BMD and trabecular bone volume compared to untreated *Tsk*<sup>+/+</sup> mice (Figure 5H and 5I), whereas miR-151-5p-depleted EVs failed to increase BMD and trabecular bone volume (Figure 5H and 5I). The numbers of adipocytes in EV/exosome-treated, but not miR-151-5p-depleted EV-treated *Tsk*<sup>+/+</sup> mouse bone marrow were significantly reduced when compared to untreated *Tsk*<sup>+/+</sup> mice, as assessed by Oil red O staining (Figure 5J). These data indicate that EVs/exosomes play an important role in the regulation of miR-151-5p levels to rescue *Tsk*<sup>+/+</sup> BMMSC function and osteopenia. To further confirm MSCT releasing EVs/exosomes to rescue *Tsk*<sup>+/+</sup> phenotypes, we blocked EV/exosome secretion *in vivo* by treating BMMSCs with *rab27a* siRNA and performed MSCT in *Tsk*<sup>+/+</sup> mice. The therapeutic effects of *rab27a*-treated BMMSCs were significantly decreased when compared to the control MSCT group, as assessed by microCT and histological analysis to show BMD and trabecular bone volume (Supplementary information, Figure S6A and S6B) and Oil red O staining to show

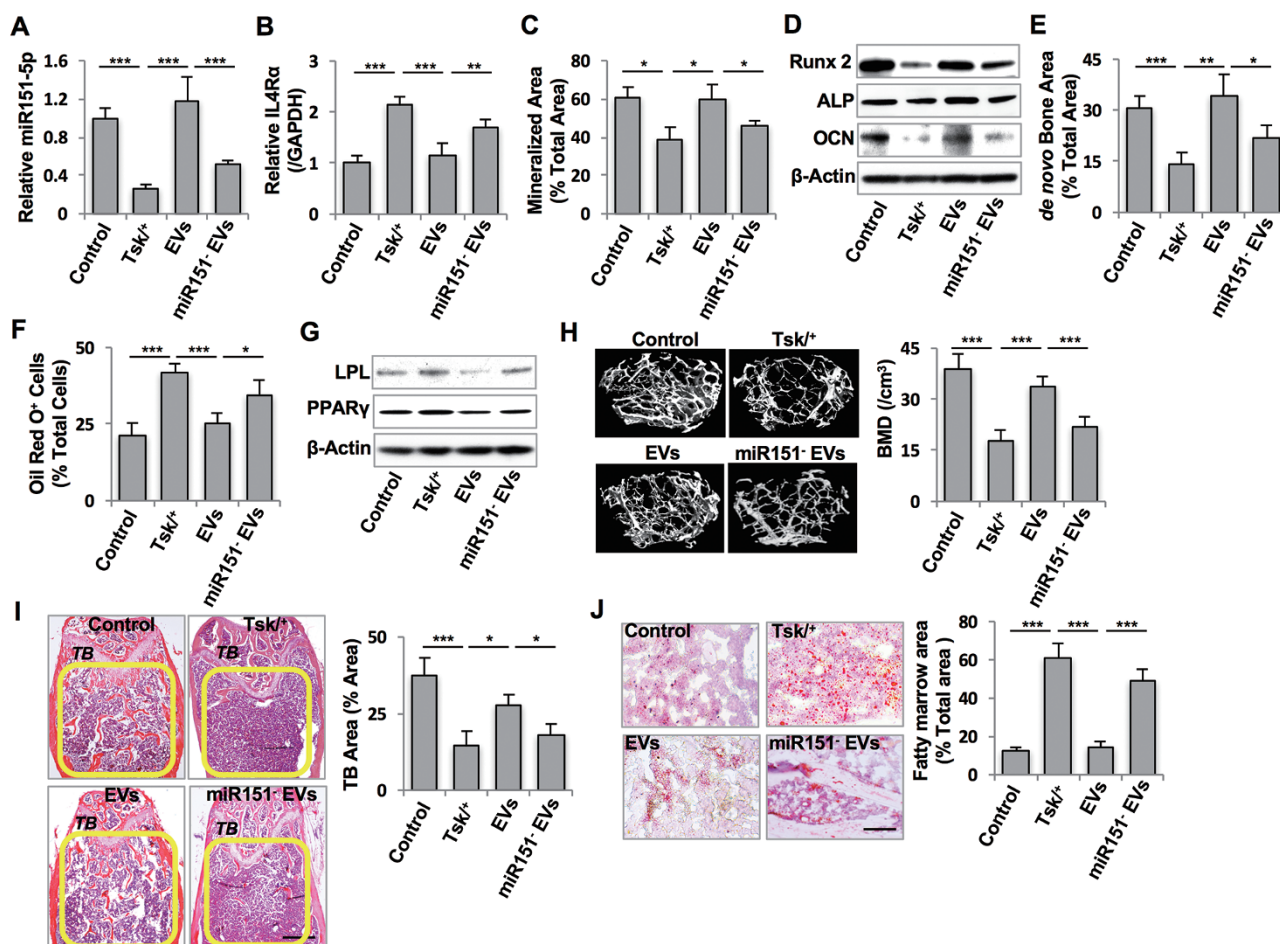


**Figure 5** Systemic infusion of exosomes rescued osteopenia in *Tsk1*<sup>+</sup> mice through miR151-5p transfer. **(A)** qPCR analysis showing the levels of miR-151-5p in WT, *Tsk1*<sup>+</sup>, exosome-treated *Tsk1*<sup>+</sup>, and miR-151-5p-depleted exosome-treated *Tsk1*<sup>+</sup> BMMSCs. **(B)** qPCR analysis showing the expression levels of *Il4ra* in WT, *Tsk1*<sup>+</sup>, exosome-treated *Tsk1*<sup>+</sup>, and miR-151-5p-depleted exosome-treated *Tsk1*<sup>+</sup> BMMSCs. **(C)** Alizarin red staining showing that WT, *Tsk1*<sup>+</sup>, exosome-treated *Tsk1*<sup>+</sup>, and miR-151-5p-depleted exosome-treated *Tsk1*<sup>+</sup> BMMSCs form mineralized nodules under osteoinductive conditions. **(D)** Western blotting analysis showing the expression levels of the osteogenic genes *Runx2*, *ALP*, and *OCN* in WT, *Tsk1*<sup>+</sup>, exosome-treated *Tsk1*<sup>+</sup>, and miR-151-5p-depleted exosome-treated *Tsk1*<sup>+</sup> BMMSCs.  $\beta$ -Actin was used as a protein loading control. **(E)** When WT, *Tsk1*<sup>+</sup>, exosome-treated *Tsk1*<sup>+</sup>, and miR-151-5p-depleted exosome-treated *Tsk1*<sup>+</sup> BMMSCs were implanted into immunocompromised mice subcutaneously, newly formed bone was observed. **(F)** The number of Oil red O<sup>+</sup> cells observed in WT, *Tsk1*<sup>+</sup>, exosome-treated *Tsk1*<sup>+</sup>, and miR-151-5p-depleted exosome-treated *Tsk1*<sup>+</sup> BMMSCs cultured under adipogenic conditions. **(G)** Western blotting showing the expression levels of adipogenic genes *PPAR $\gamma$*  and *LPL* in WT, *Tsk1*<sup>+</sup>, exosome-treated *Tsk1*<sup>+</sup>, and miR-151-5p-depleted exosome-treated *Tsk1*<sup>+</sup> BMMSCs cultured under adipogenic conditions. **(H)** MicroCT analysis showing BMD and TB area in distal femurs of WT, *Tsk1*<sup>+</sup>, exosome-treated *Tsk1*<sup>+</sup>, and miR-151-5p-depleted exosome-treated *Tsk1*<sup>+</sup> mice. **(I)** H&E staining showing TB volume (yellow-circled area) in WT, *Tsk1*<sup>+</sup>, exosome-treated *Tsk1*<sup>+</sup>, and miR-151-5p-depleted exosome-treated *Tsk1*<sup>+</sup> mouse distal femurs. Scale bar, 1 mm. **(J)** Histological images of distal femurs showing the number of adipocytes in WT, *Tsk1*<sup>+</sup>, exosome-treated *Tsk1*<sup>+</sup>, and miR-151-5p-depleted exosome-treated *Tsk1*<sup>+</sup> mouse bone marrow based on Oil red O staining. Scale bar, 50  $\mu$ m. All experimental data were verified in at least three independent experiments. Error bars represent the s.d. from the mean values. \*\*\* $P$  < 0.005; \*\* $P$  < 0.001; \* $P$  < 0.05.

adipocytes in *Tsk1*<sup>+</sup> mouse bone marrow (Supplementary information, Figure S6C).

*Overexpression of miR-151-5p rescues disease pheno-*

*types in Tsk1+ mice*

In light of miR-151-5p negatively regulating *IL4R $\alpha$*  expression in *Tsk1*<sup>+</sup> BMMSCs, we next assessed the effects of overexpressing miR-151 in *Tsk1*<sup>+</sup> mice by ad-

enoviral vector with a green fluorescent protein (GFP) reporter (Ad-miR-151). Ad-miR151 ( $2 \times 10^9$  p.f.u.) or an empty vector (Ad-GFP) was injected into *Tsk*<sup>+/+</sup> mice three times a week for up to 4 weeks (Figure 6A). Forty-eight hours after the last injection, we used immunofluorescent analysis to show GFP expression in Ad-

miR-151-treated *Tsk*<sup>+/+</sup> bone marrow cells (Figure 6B). Ad-miR-151-treated *Tsk*<sup>+/+</sup> BMMSCs were collected to show elevation of the intracellular levels of miR-151-5p (Figure 6C) and reduced expression levels of *Il4ra* (Figure 6D). Osteogenic differentiation of BMMSCs from Ad-miR-151-treated *Tsk*<sup>+/+</sup> mice was markedly improved

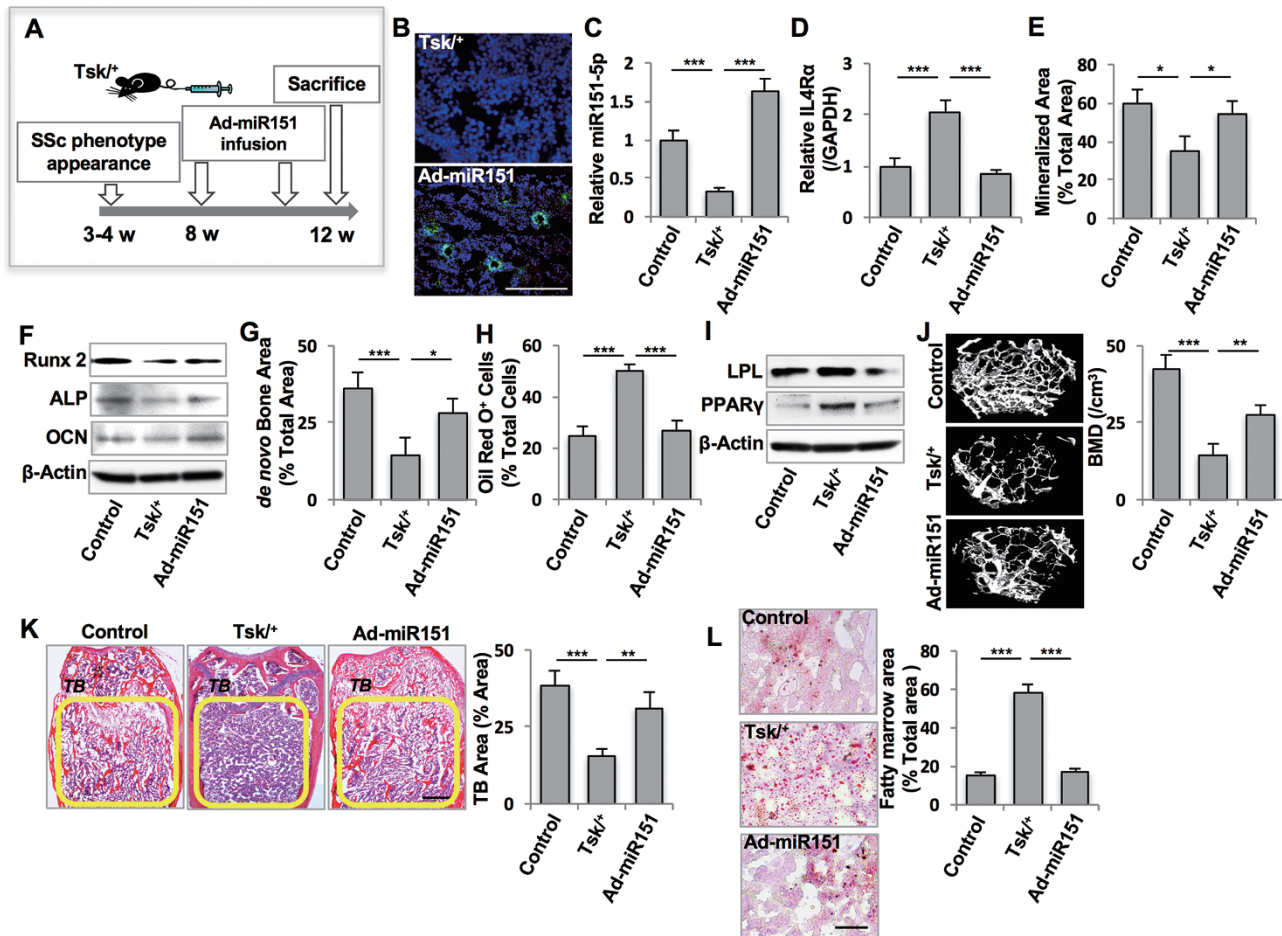


**Figure 6** Adenovirus-mediated miR-151-5p overexpression rescued impaired *Tsk*<sup>+/+</sup> BMMSCs. **(A)** Experimental outline describing the use of Ad-miR-151 to treat *Tsk*<sup>+/+</sup> mice ( $n = 6$  per group). **(B)** Ad-miR-151-GFP was observed in bone marrow cells of *Tsk*<sup>+/+</sup> mice. Scale bar, 25  $\mu$ m. **(C)** qPCR analysis showing the levels of miR-151-5p in WT, Ad-GFP, and Ad-miR-151-treated *Tsk*<sup>+/+</sup> BMMSCs. **(D)** qPCR analysis showing the expression levels of *Il4ra* in WT, Ad-GFP, and Ad-miR-151-treated *Tsk*<sup>+/+</sup> BMMSCs. **(E)** Alizarin red staining showing mineralized nodule formation in WT, Ad-GFP, and Ad-miR-151-treated *Tsk*<sup>+/+</sup> BMMSCs cultured under osteoinductive conditions. **(F)** Western blotting showing the expression levels of the osteogenic genes *Runx2*, *ALP*, and *OCN* in WT, Ad-GFP, and Ad-miR-151-treated *Tsk*<sup>+/+</sup> BMMSCs.  $\beta$ -Actin was used as a protein loading control. **(G)** When WT, Ad-GFP, and Ad-miR-151-treated *Tsk*<sup>+/+</sup> BMMSCs were subcutaneously implanted into immunocompromised mice, newly formed bone was observed. **(H)** The number of Oil red O<sup>+</sup> cells in WT, Ad-GFP, and Ad-miR-151-treated *Tsk*<sup>+/+</sup> BMMSCs under the adipogenic conditions. **(I)** Western blotting showing the expression levels of adipogenic genes *PPAR $\gamma$*  and *LPL* in WT, Ad-GFP, and Ad-miR-151-treated *Tsk*<sup>+/+</sup> BMMSCs cultured under adipogenic conditions. **(J)** MicroCT analysis showing BMD and TB area in distal femurs of WT, Ad-GFP, and Ad-miR-151-treated *Tsk*<sup>+/+</sup> mice. **(K)** H&E staining showing TB volume (yellow-circled area) in WT, Ad-GFP, and Ad-miR-151-treated mouse distal femurs. Scale bar, 1 mm. **(L)** Histological images of distal femurs showing the number of adipocytes in WT, Ad-GFP, and Ad-miR-151-treated mouse bone marrow, assessed by Oil red O staining. Scale bar, 50  $\mu$ m. All experimental data were verified in at least three independent experiments. Error bars represent the s.d. from the mean values. \*\*\* $P < 0.005$ ; \*\* $P < 0.001$ ; \* $P < 0.05$ .

when compared to the Ad-GFP-treated *Tsk*<sup>+</sup> BMMSCs, as analyzed by alizarin red staining to show elevated mineralized nodule formation (Figure 6E), western blotting to show increased expression of the osteogenic genes *Runx2*, *ALP*, and *OCN* (Figure 6F), and *in vivo* BMMSC implantation to show elevated new bone formation (Figure 6G). In contrast, BMMSCs isolated from Ad-miR-151-treated *Tsk*<sup>+</sup> mice showed significantly less adipogenic differentiation than BMMSCs from Ad-GFP-treated *Tsk*<sup>+</sup> mice, as shown by a decreased number of Oil red O-positive cells and downregulation of *PPAR $\gamma$*  and *LPL* (Figure 6H and 6I). Histological and microCT analysis showed that Ad-miR-151 treatment elevated BMD and trabecular bone volume compared to Ad-GFP-treated *Tsk*<sup>+</sup> mice (Figure 6J and 6K). The number of adipocytes in the bone marrow of Ad-miR-151-treated *Tsk*<sup>+</sup> mice was significantly reduced compared to Ad-GFP-treated *Tsk*<sup>+</sup> mice, as assessed by Oil red O staining (Figure 6L). To examine whether overexpressing miR151-5p can increase therapeutic effects of EVs, we treated BMMSCs with Ad-miR151 to generate miR151-overexpressed (miR151-OE) EVs and subsequently infused these EVs into *Tsk*<sup>+</sup> mice. Treatment with EVs from  $0.2 \times 10^6$  BMMSCs is considered a standard dosage to generate a therapeutic response. Therefore, we infused 10% of this standard dose of EVs (i.e., EVs from  $0.02 \times 10^6$  BMMSCs) from miR151-5p-overexpressed BMMSCs or control WT BMMSCs into *Tsk*<sup>+</sup> mice to examine whether miR151-5p overexpression in BMMSCs could elevate the therapeutic effects of EVs. The results showed that this small dose of EVs from miR151-overexpressed BMMSCs, but not from WT BMMSCs, had similar therapeutic effects to those observed in EVs from the  $0.2 \times 10^6$  BMMSCs group, as assessed by microCT and histological analysis (Supplementary information, Figure S7A and S7B) and Oil red O staining (Supplementary information, Figure S7C).

Next, we examined whether systemic infusion of Ad-miR-151 rescues autoimmune and connective tissue disorders in *Tsk*<sup>+</sup> mice, which represent major phenotypes of SSc. To evaluate skin fibrosis, we found that skin hypodermal thickness was reduced to a level equivalent to the control group after systemic administration of Ad-miR-151 (Figure 7A). *Tsk*<sup>+</sup> mice showed increased levels of antinuclear antibody (ANA), anti-double strand DNA (dsDNA) IgG and IgM antibodies, creatinine in serum, and urine proteins (Figure 7B-7F). When compared to the Ad-GFP treatment group, Ad-miR-151 treatment significantly reduced the levels of ANA, dsDNA IgG and IgM, serum creatinine, and urine protein in *Tsk*<sup>+</sup> mice (Figure 7B-7F). As mature miR-151-5p is able to directly target *Il4ra*, a key component of T<sub>H</sub>2 cytokine

signaling in the regulation of fibrotic tissue deposition and bone homeostasis in SSc [9-11], we hypothesized that systemic Ad-miR-151 infusion downregulates T<sub>H</sub>2 differentiation in *Tsk*<sup>+</sup> mice. To evaluate the efficiency of *in vivo* Ad-miR-151 treatment, serum levels of miR-151-5p were examined by qPCR and we found a markedly decreased level of miR-151-5p in *Tsk*<sup>+</sup> mice compared to control littermates (Supplementary information, Figure S8A). Ad-miR-151 treatment significantly elevated serum levels of miR-151-5p (Supplementary information, Figure S8A). Flow cytometric analysis showed that *Tsk*<sup>+</sup> mice have significantly increased levels of T<sub>H</sub>2 cells (Supplementary information, Figure S8B) and T<sub>H</sub>17 cells (Supplementary information, Figure S9A), reduced levels of regulatory T cells (Tregs), and unaltered levels of T<sub>H</sub>1 cells compared with control littermates (Supplementary information, Figure S9B and S9C). Ad-miR-151 treatment markedly reduced the levels of T<sub>H</sub>2 cells (Supplementary information, Figure S8B), but not T<sub>H</sub>17 cells, T<sub>H</sub>1 cells, or Tregs (Supplementary information, Figure S9A-S9C). ELISA confirmed that Ad-miR-151 treatment significantly reduced serum levels of IL4 in *Tsk*<sup>+</sup> mice (Supplementary information, Figure S8C). Moreover, we found that Ad-miR-151 treatment significantly reduced CD4<sup>+</sup>IL4<sup>+</sup> T<sub>H</sub>2 cell infiltration, a major pathological phenotype in *Tsk*<sup>+</sup> mice [9-11], as confirmed by IF staining (Supplementary information, Figure S9D). To further examine the relationship between miR-151-5p and reduced T<sub>H</sub>2 cell differentiation, we infected naive *Tsk*<sup>+</sup> CD4 T cells with Ad-miR-151 to assess the effects on T helper cell differentiation, activated under either non-polarized T<sub>H</sub>0 or T<sub>H</sub>2 conditions. Ad-miR-151 treatment promoted a marked increase in miR-151-5p in differentiated T cells under T<sub>H</sub>0 or T<sub>H</sub>2 conditions (Supplementary information, Figure S8D). In the presence of increased miR-151-5p, we observed downregulation of the T<sub>H</sub>2 genes, *Il4* and *Gata3*, compared to T cells infected with control Ad-GFP (Supplementary information, Figure S8E). ELISA further confirmed that Ad-miR-151 treatment reduced T<sub>H</sub>2 cytokine IL4 production under T<sub>H</sub>0 or T<sub>H</sub>2 conditions (Supplementary information, Figure S8F). Flow cytometric analysis showed that Ad-miR-151 significantly decreased T<sub>H</sub>2 cells under T<sub>H</sub>0 or T<sub>H</sub>2 conditions compared with Ad-GFP treatment (Supplementary information, Figure S8G). These data prompted us to examine whether osteoclast numbers rebound after MSCT as a direct result of the transplant itself (transfer of miR-151-5p). We isolated osteoclast precursors from bone marrow and induced them to differentiate into osteoclasts by treating them with M-CSF and RANKL. The results showed that IL-4 treatment significantly inhibited osteoclastogenesis, which mimics the microenvironment in *Tsk*<sup>+</sup> mice. Over-

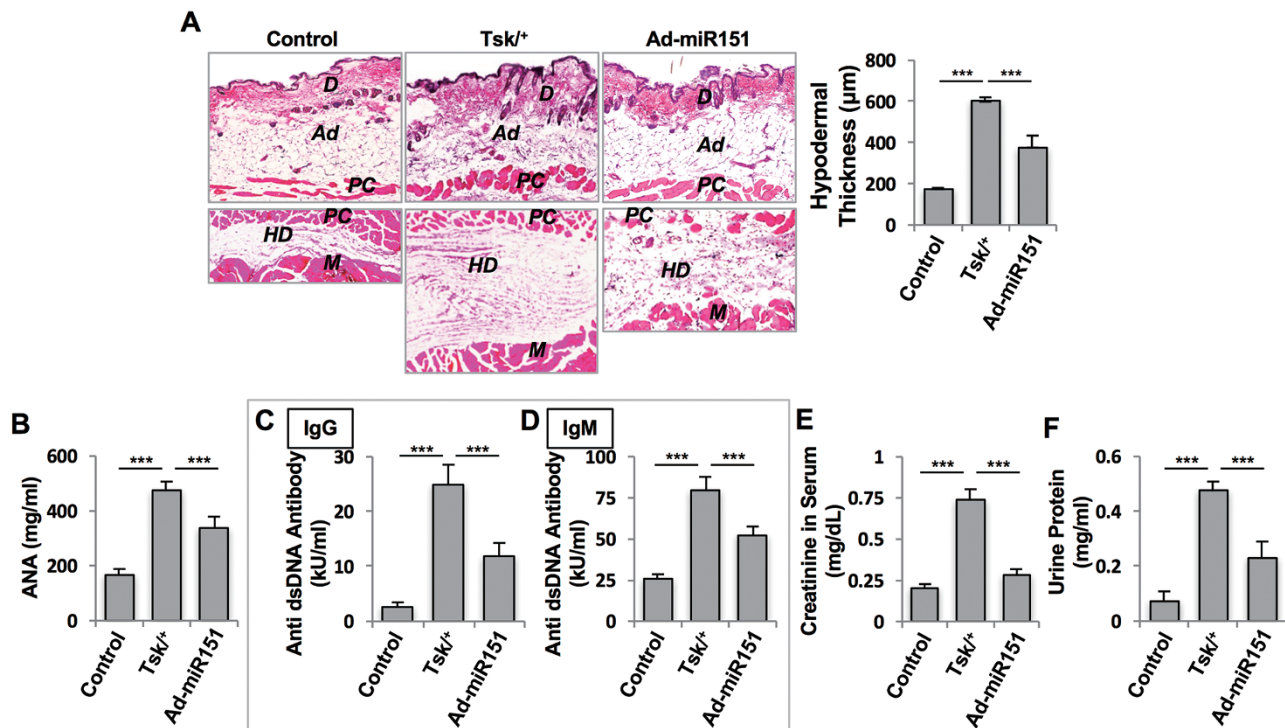


**Figure 7** Ad-miR-151 treatment ameliorated skin fibrosis and autoimmune index in *Tsk*<sup>+/+</sup> mice. **(A)** Hypodermal thickness was significantly increased in *Tsk*<sup>+/+</sup> mice compared to the WT group ( $n = 6$  each group). Ad-miR-151 treatment significantly reduced the hypodermal thickness in *Tsk*<sup>+/+</sup> mice. **(B–D)** *Tsk*<sup>+/+</sup> mice showed elevated levels of ANA **(B)** and anti-double-strand DNA antibodies IgG **(C)** and IgM **(D)** when compared to control littermates. Ad-miR-151 treatment reduced the levels of ANA **(B)** and anti-double-strand DNA antibodies IgG **(C)** and IgM **(D)**. **(E)** Serum creatinine levels were significantly increased in *Tsk*<sup>+/+</sup> mice. After Ad-miR-151 treatment, creatinine levels were significantly decreased to the level similar to the control group. **(F)** The concentration of urine protein was significantly increased in *Tsk*<sup>+/+</sup> mice. Ad-miR-151 treatment reduced the levels of urine protein. The results were representative of three independent experiments. Ad, adipose; ANA, antinuclear antibody; D, dermis; HD, hypodermis; M, muscle; PC, panniculus carnosus. Scale bar, 50 μm. \*\*\* $P < 0.005$ .

expression of miR151-5p with Ad-miR151 treatment inhibited IL4R $\alpha$  expression in osteoclast precursors, along with significantly increased osteoclastogenesis (Supplementary information, Figure S10). These data suggest that MSCT may directly transfer miR151-5p via EVs to increase osteoclast numbers in *Tsk*<sup>+/+</sup> mice. Collectively, these data reveal that MSCT ameliorates disease phenotypes in *Tsk*<sup>+/+</sup> mice through downregulating IL4R $\alpha$  signaling in recipient BMMSCs to rescue impaired osteo/adipogenic lineage differentiation via exosome-mediated miR-151-5p transfer (Supplementary information, Figure S11), suggesting that miR-151-5p treatment may be a target-specific therapy for SSc.

#### *SSc patients show decreased serum levels of miR-151-5p and elevated expression of IL4R $\alpha$ /mTOR cascade in BMMSCs*

In order to confirm that miR-151-5p-mediated downregulation of IL4R $\alpha$ /mTOR signaling is relevant to SSc

in human patients, we conducted a pilot clinical investigation to assess whether diminished miR-151-5p levels and activated IL4R $\alpha$ /mTOR signaling can be observed in SSc patients. Twenty patients diagnosed with SSc and 20 age- and gender-matched normal controls were enrolled in this study (Supplementary information, Table S2). qPCR analysis showed that serum levels of miR-151-5p were markedly decreased in SSc patients compared to normal controls (Figure 8A). Flow cytometric analysis showed that CD4<sup>+</sup>IL4<sup>+</sup> T<sub>H</sub>2 cells were significantly increased in the peripheral blood of SSc patients compared to the control group (Figure 8B). ELISA further confirmed that serum IL4 levels were significantly elevated in SSc patients (Figure 8C). In addition, we found that SSc patients had significantly elevated levels of serum TGF $\beta$  and upregulation of *Il4ra* in BMMSCs by ELISA and qPCR analysis, respectively (Figure 8D and 8E). As mTOR complex 2 (TORC2) may act upstream of TORC1 in *Tsk*<sup>+/+</sup> BMMSCs [11], we showed that BMMSCs from

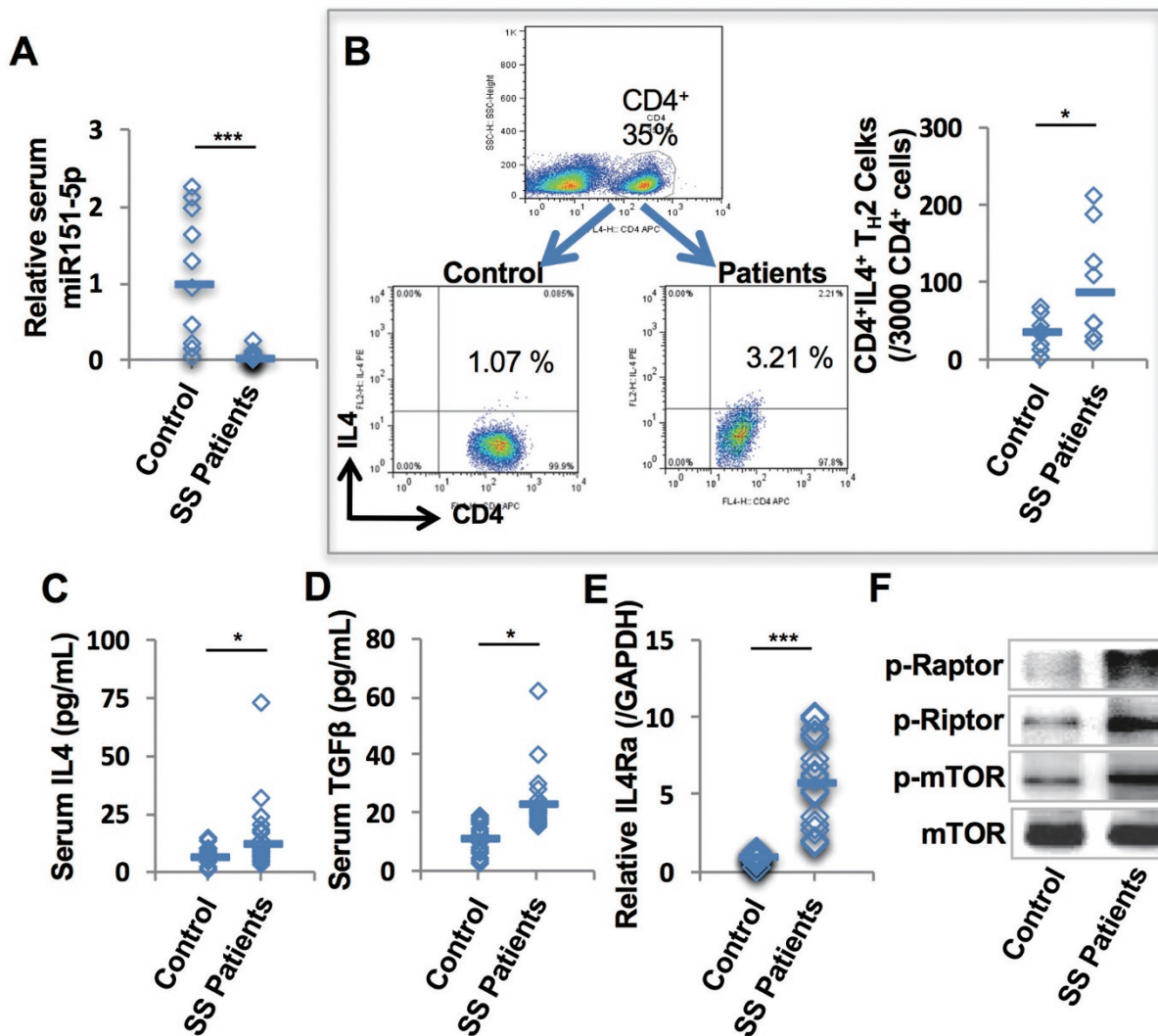


**Figure 8** Systemic sclerosis patients showed decreased serum levels of miR-151-5p and elevated expression levels of IL4R $\alpha$  and mTOR in BMMSCs. **(A)** qPCR analysis showed the serum levels of miR-151-5p in SSc patients ( $n = 13$ ) and normal controls ( $n = 11$ ). **(B)** Flow cytometric analysis showed elevated levels of T<sub>H2</sub> cells in peripheral blood of SSc patients compared to normal controls ( $n = 9$  per group). **(C)** ELISA showed increased serum levels of IL4 in SSc patients compared to normal controls ( $n = 20$ ). **(D)** ELISA showed that SSc patients ( $n = 20$ ) had increased serum levels of TGF $\beta$  compared to normal controls. **(E)** qPCR analysis showing that BMMSCs from SSc patients ( $n = 20$ ) had upregulated expression of *Il4ra*. **(F)** Western blot analysis showed upregulation of p-Raptor, p-Rictor, and p-mTOR in BMMSCs from SSc patients. Representative results were from three independent experiments. Error bars represent the s.d. from the mean values. \*\*\* $P < 0.005$ ; \* $P < 0.05$ .

SSc patients had upregulated expression of p-Raptor, p-Rictor, and p-mTOR (Figure 8F).

## Discussion

As the first MSCT was successfully performed in severe acute GvHD patients in 2004 [12], MSCs from different sources have been widely utilized to treat various diseases [44–46]. Previous studies proposed multiple

mechanisms may contribute to the success of MSC-based immune therapies such as secretion of cytokines/chemokines, cell-cell interactions, and epigenetic regulation [24, 28, 36]. Recently, allogenic MSC-based cell therapy showed efficacy in a HOCl-induced SSc murine model, which is a closer match to the human disease [47, 48]. These studies, combined with several recent publications, suggest that the safety and efficacy of allogenic MSC-based therapy make it a promising approach in

treating autoimmune and non-autoimmune diseases [49–51]. MSCT not only rescues osteoporosis in *Tsk*<sup>+/+</sup> mice, but also rescues the autoimmune phenotype and skin fibrosis in *Tsk*<sup>+/+</sup> mice [28]. In addition, we observed that osteoclast numbers rebound after MSCT. It is possible that MSCT involves multiple mechanisms to rescue disease phenotypes in *Tsk*<sup>+/+</sup> mice and other autoimmune disorders. Due to the nature of allogeneic transplant, there is little evidence to support the persistence of the graft in the recipient. Transferring miRNA and functional cellular components may be one of the therapeutic mechanisms mediated by MSCT. In this study, we showed that systemic administration of BMMSCs transfers miR-151-5p to *Tsk*<sup>-/-</sup>-recipient BMMSCs to rescue impaired osteo/adipogenic differentiation of recipient cells. Previous studies indicated that exosomes could serve as a vehicle to transfer miRNAs between cells [34, 52] to regulate gene expression and have the potential to offer therapies for stroke, liver fibrosis, and cardiovascular diseases [53–55]. We found that recipient *Tsk*<sup>+/+</sup> BMMSCs are able to take miR-151-5p/exosomes from donor MSCs and reuse miR-151-5p to downregulate *IL4Rα* expression, resulting in the improvement of recipient cell function. In addition, MSCs are capable of producing large amounts of exosomes [56]. Therefore, exosome/miRNA transfer may play a significant role in MSCT-mediated therapies. It appears that MSCT exerts therapeutic effects through multiple mechanisms of interaction with recipient microenvironments; however, the detailed mechanism by which the recipient microenvironment affects MSCT-mediated exosome transfer is unknown.

Differentially expressed miRNA profiles related to inflammation and fibrosis have been identified in SSc patients [57, 58]. Previous studies suggest that miRNAs mainly modulate fibrosis-related genes such as collagens, metalloproteinases, integrins, TGFβ, DNA methyltransferase 1, and toll-like receptors [59], which could partially explain why SSc phenotypes display marked heterogeneity and imply complex interplay between different pathogenic processes. Among these complex pathophysiological factors, T helper cell homeostasis is generally biased toward T<sub>H</sub>2 with the production of high levels of cytokines IL4 and IL13 in SSc [9]. Disruption of IL4 or *IL4Rα* can rescue the fibrosis and osteopenia phenotypes, suggesting that IL4/*IL4Rα* signaling may have an essential role in the disease pathogenesis [10, 11]. Accordingly, we decided to use T<sub>H</sub>2-highly activated *Tsk*<sup>+/+</sup> mice as an SSc mouse model in this study, even though the *Tsk*<sup>+/+</sup> model does not perfectly mimic the clinical and immunological features of human SSc. In the present study, we identified a novel target, miR-151-5p, which plays a critical role in regulating BMMSC differ-

entiation via suppressing *IL4Rα*. Through transfection of miR151-5p mimic or adenovirus-mediated miR-151-5p overexpression, *Tsk*<sup>+/+</sup> BMMSC function is largely improved, implying that miR-151-5p-based therapy may be a target-specific approach to treat SSc patients. Previous studies showed that multiple miRNAs are capable of regulating the osteogenic differentiation of BMMSCs and maintaining bone homeostasis [60, 61]. Here we found that miR-151-5p mediated a lineage switch between osteogenic and adipogenic differentiation and rescued the osteopenia phenotype in *Tsk*<sup>+/+</sup> mice. Interestingly, human miR-151-5p is able to target *hIl4ra* expression in human BMMSCs. Also, SSc patients showed significantly reduced serum levels of miR-151-5p, raising the possibility of translating our findings to the clinic. A major challenge in clinical practice is new biomarker discovery, which can be used for better disease diagnosis and classification. Notably, miR-151-5p may be able to serve as a biomarker for SSc diagnosis.

Gene therapy has been widely used to replace defective protein-coding genes in many genetic diseases. Given the crucial roles of miRNAs in regulating gene expression and disease development, miRNAs are considered as potential therapeutic targets for gene therapy. Recently, miRNA-based gene therapy has been established in some diseases that may be caused by the loss or reduced expression of a particular miRNA [62]. Due to the inefficient delivery or degradation of miRNAs, viral vectors encoding short hairpin RNAs, which are processed in the cell into mature miRNAs, are a promising alternative method of miRNA delivery [63]. In this study, we overexpressed miR-151 *in vivo* using an adenoviral vector, which produces mature miR-151-5p in recipient cells. Overexpression of miR-151-5p significantly reduced *Il4ra* expression and rescued osteopenia in *Tsk*<sup>+/+</sup> mice, which encouraged us to examine whether adenovirus-mediated miR-151-5p overexpression could affect other organs. Indeed, SSc morbidity and mortality are strongly related to fibrosis and vasculopathy. Osteopenia may not be one of the most challenging issues in SSc. Our data indicated that Ad-miR151 treatment successfully reduced T<sub>H</sub>2 cell differentiation and decreased T-cell infiltration in the hyperdermal area, suggesting that miR-151-5p-based gene therapy can achieve therapeutic effects in multiple organs in *Tsk*<sup>+/+</sup> mice. To carry out both effective and safe miR151-5p-based gene therapy, its potential off-target effects need to be further explored in future study.

Dysfunction of BMMSCs in *Tsk*<sup>+/+</sup> mice caused by altered IL4/*IL4Rα* signaling results in an osteopenia phenotype, suggesting that osteo-immunological effect on stem cell homeostasis contributes to the SSc phenotype.

Upregulation of osteogenesis and downregulation of adipogenesis by miR-151-5p mimic treatment via inhibition of *Il4ra* expression may help to rebuild BMMSC function and bone marrow homeostasis. miR151-5p can serve as a promising biomarker for SSc diagnosis and a therapeutic target in SSc treatment. Given the extensive roles of MSCT in treating various autoimmune diseases, it is possible that other miRNAs can be transferred to target other specific signaling pathways.

## Materials and Methods

### Animals

Female C57BL/6J and B6.Cg-*Fbn1*<sup>Tsk/J</sup> (*Tsk*<sup>+</sup>) mice were purchased from Jackson Lab and maintained in a C57BL/6J background at least 10 backcrosses. Age-matched female littermates were used in all experiments. Female immunocompromised nude mice (Beige *nu/nu* XIDIII) were purchased from Harlan. All animal experiments were performed under institutionally approved protocols for the use of animal research (University of Pennsylvania protocol number 805478).

### Isolation of mouse BMMSCs

A single suspension of bone marrow-derived all nuclear cells (ANCs,  $15 \times 10^6$ ) from femurs was seeded in 100 mm culture dishes (Corning) and incubated at 37 °C with 5% CO<sub>2</sub>. After 48 h, non-adherent cells were removed, and adherent cells were cultured for additional 14 days in alpha minimum essential medium ( $\alpha$ -MEM, Invitrogen) supplemented with 20% fetal bovine serum (FBS), 2 mM L-glutamine (Invitrogen), 55  $\mu$ M 2-mercaptoethanol (Invitrogen), 100 U/ml penicillin, and 100  $\mu$ g/ml streptomycin (Invitrogen). These adherent single colonies were passaged at passage one with frequent medium changes to eliminate potential hematopoietic cell contamination [64, 65]. Since previous publications indicated that numerous passages of murine BMMSCs in atmospheric oxygen culture conditions can lead to spontaneous transformation both *in vitro* and *in vivo* [66–68], we used passage one mouse BMMSCs in this study. For CFU-F assay,  $1 \times 10^6$  single-suspension ANCs were seeded in T25 cell culture flasks (Corning). After 16 days, the cultures were washed with PBS and stained with 1% toluidine blue solution with 2% paraformaldehyde (PFA, Sigma-Aldrich). The cell clusters were counted under microscopy and those with more than 50 cells were considered as colonies.

### Allogenic MSCT of SSc mice

BMMSCs, isolated from C57BL/6J mice at passage one, were suspended in 200  $\mu$ l PBS and intravenously infused into *Tsk*<sup>+</sup> SSc mice ( $0.1 \times 10^6$  cells per 10 g body weight) at 8 weeks of age. In the control group, *Tsk*<sup>+</sup> mice received PBS. Background-matched WT mice were infused with PBS intravenously as positive controls.

### MicroCT analysis

After being harvested and fixed in 4% PFA, femurs were analyzed using a high-resolution Scanco  $\mu$ CT50 scanner (Scanco Medical AG, Bruttisellen, Switzerland). The specimens were scanned using a voxel size of 20  $\mu$ m at 70 kVp and 200  $\mu$ A. Data-sets were analyzed using Amira 5.3.1 software (Visage Imaging, Berlin, Germany) for reconstructing images and measuring BMD.

### Histology

To assess trabecular bone and bone marrow areas, femurs were fixed in 4% PFA and then decalcified with 5 % EDTA (pH 7.4), followed by paraffin embedding. Paraffin sections 6  $\mu$ m in thickness were stained with hematoxylin and eosin (H&E) and analyzed using NIH ImageJ software. For immunohistochemistry staining, paraffin-embedded sections were incubated with the ALP or IL4 antibodies (Santa Cruz Biotechnology, Inc., 1:400) at 4 °C for overnight, and then stained with VECTASTAIN UNIVERSAL elite ABC kit and ImmPACT VIP peroxidase Substrate Kit (VECTOR) according to the manufacturer's instruction. For osteoclast activity quantification, TRAP-positive cells were identified as mature osteoclasts on the bone surface. De-paraffinized sections were re-fixed with a mixture of 50% ethanol and 50% acetone for 10 min, and then incubated in the freshly made TRAP solution for staining with 1.6% naphthol AS-BI phosphate in N, N-dimethylformamide, 0.14% fast red-violet LB diazonium salt, 0.097% tartaric acid, and 0.04% MgCl<sub>2</sub> in 0.2 M sodium acetate buffer at pH 5.0 for 10 min at 37 °C under a shield. Samples were counterstained with toluidine blue. All reagents for TRAP staining were purchased from Sigma-Aldrich. For double calcein labeling histomorphometric analysis, the mice were intraperitoneally injected with calcein (Sigma, 15 mg/kg body weight) prepared in 2% sodium bicarbonate solution at 10 days and 3 days before killing. Bone dynamic histomorphometric analyses for MAR and BFR/BS were performed according to the standardized nomenclature for bone histomorphometry under fluorescence microscopy (Olympus IX71, Japan).

### ELISA

Peripheral blood serum was collected and analyzed using mouse ELISA Ready-SET-GO kits (eBioscience) for sRANKL, IFN $\gamma$ , IL4, IL17, and IL10 protein levels, according to the manufacturer's instructions. CTX levels were analyzed with a mouse C-telopeptide of type I collagen ELISA kit (Novateinbio), according to the manufacturer's instructions. Human IL4 and TGF $\beta$  protein levels were analyzed using ELISA Ready-SET-GO kits (eBioscience), according to the manufacturer's instructions. Mouse ANA, anti-dsDNA IgG, anti-dsDNA IgM, and creatinine (Alpha Diagnosis) were measured using commercially available kits according to manufacturer's instructions.

### *In vitro* osteogenic differentiation

BMMSCs were cultured under osteogenic inductive conditions, including 2 mM  $\beta$ -glycerophosphate (Sigma-Aldrich), 100  $\mu$ M L-ascorbic acid 2-phosphate (Wako), and 10 nM dexamethasone (Sigma-Aldrich) in the growth medium. After 3 weeks of induction, matrix mineralization was detected by 1% Alizarin Red S (Sigma-Aldrich) staining, and the stained positive areas were quantified using NIH ImageJ software and shown as a percentage of the total area.

### Co-culture of WT BMMSCs with *Tsk*<sup>+</sup> BMMSCs

A transwell system for 12-well plates (Corning) was used for co-culture experiments. *Tsk*<sup>+</sup> BMMSCs ( $0.2 \times 10^6$  cells per well) were loaded in each lower chamber. WT BMMSCs ( $0.2 \times 10^6$  cells per well) transfected with Cy3 red fluorescent dye-labeled miR-151-5p, Rab27a siRNA, or negative control siRNA were loaded in each upper chamber. After 3 days of co-culture, *Tsk*<sup>+</sup> BMMSCs

were used for microscopic imaging, total RNA isolation, protein isolation, and osteogenic differentiation analysis.

#### Western blotting

Cells were washed with PBS and lysed in M-PER mammalian protein extraction reagent (Thermo) with protease and phosphatase inhibitors (Roche). Protein levels were quantified using a protein concentration assay (Bio-Rad Laboratories). Twenty  $\mu\text{g}$  of proteins were separated by SDS-PAGE (Invitrogen) and transferred to 0.2  $\mu\text{m}$  nitrocellulose membranes (Millipore). The membranes were then blocked with 5% non-fat dry milk and 0.1% Tween-20 for 1 h, followed by incubation overnight with primary antibodies diluted in blocking solution. Antibodies to mouse ALP (sc-28904), LPL (sc-32382), PPAR $\gamma$  (sc-7273), IL4R (sc-684), and PI3K-p110 (sc-7189) were purchased from Santa Cruz Biotechnology, Inc. Antibodies to human Runx2 (sc-10758), ALP (sc-28904), and OCN (sc-18319) were purchased from Santa Cruz Biotechnology, Inc. Antibodies to phosphor-mTOR (Ser2448, 5536), mTOR (2983), phospho-Akt (Ser473, 9271), Akt (9272), phosphor-P70S6K (T389, 9243; S371, 9208), phosphor-Rictor (3806), and phosphor-Raptor (2083) were obtained from Cell Signaling Technology. Antibodies to mouse Runx2 (ab76956), OCN (Ab10911), and  $\beta$ -Actin (A5441) were purchased from Abcam, Millipore, and Sigma-Aldrich. The membranes were then washed and incubated for 1 h in HRP-conjugated secondary antibody (Santa Cruz Biotechnology, Inc.) diluted in blocking solution. Immunoreactive proteins were detected using SuperSignal West Pico Chemiluminescent Substrate (Thermo) and BioMax film (Kodak).

#### In vivo BMMSC implantation

$4.0 \times 10^6$  BMMSCs, isolated from C57BL/6J, *Tsk*<sup>+</sup>, MSCT, exosome-treated, and Ad-miR151-treated mice, were mixed with HA/TCP ceramic powders (40 mg, Zimmer Inc.) and implanted into 8-week-old nude mice subcutaneously. At 8 weeks post implantation, the transplants were harvested, fixed in 4% PFA, and decalcified with 5% EDTA, followed by paraffin embedding. The 6  $\mu\text{m}$  paraffin sections were stained with H&E, and bone volume was quantified by NIH ImageJ software as a percentage of the total area.

#### Adipogenic differentiation

For adipogenesis, BMMSCs were cultured under adipogenic inductive conditions, in growth medium containing 500 nM isobutylmethylxanthine (Sigma-Aldrich), 60  $\mu\text{M}$  indomethacin (Sigma-Aldrich), 500 nM hydrocortisone (Sigma-Aldrich), 10  $\mu\text{g}/\text{ml}$  insulin (Sigma-Aldrich), and 100 nM L-ascorbic acid phosphate. At 7 days post induction, the adipocytes were stained with Oil red O (Sigma-Aldrich), and positive cells were quantified under microscopy and shown as a number out of the total cells.

#### In vivo Oil red O staining

To quantify the adipocytes surrounding the trabecular areas, femurs were fixed in 4% PFA and decalcified with 5% EDTA (pH 7.4), followed by cryosectioning and staining with Oil Red-O solution. Positive areas were quantified under microscopy and shown as a percentage of the total area.

#### Flow cytometry

For intercellular staining, T cells were stained with 1  $\mu\text{g}$  anti-

CD4-PerCP and CD25-APC antibodies for 30 min on ice. After washing and centrifuging, cells were stained with 1  $\mu\text{g}$  anti-IFN $\gamma$ -APC, IL4-PE, IL17-PE, or Foxp3-PE antibodies using a Foxp3 staining buffer kit (eBioscience). All antibodies were purchased from BD Bioscience. After staining, all samples were analyzed using FACS<sup>Calibur</sup> with CellQuest software (BD Bioscience).

#### Real-time PCR

Total RNA was isolated from the cultured cells using the miRNeasy Mini Kit (Qiagen) according to the manufacturer's instructions. Total RNA from culture medium, serum, and bone marrow supernatant was isolated using the miRNeasy Serum/Plasma Kit (Qiagen). For real-time PCR of mRNA, the cDNA was synthesized using SuperScript III (Life Technologies). The real-time PCR was performed using SYBR green supermix (Bio-Rad, Hercules, CA, USA) and gene-specific primers. For real-time PCR of mature miRNA, cDNA was synthesized using the miScript II RT Kit (Qiagen). Real-time PCR was performed using the miScript SYBR Green PCR Kit (Qiagen). RUN6 was used as an endogenous control for BMMSCs. MiR-39 was used as spike-in control for culture medium, serum, and bone marrow (Qiagen). Real-time PCR was detected on a CFX96 Real-Time PCR System (Bio-Rad).

#### Extracellular vesicles treatment for *Tsk*<sup>+</sup> BMMSCs

EVs were isolated from C57BL/6J murine-derived BMMSCs by ultracentrifuge. MSCs were cultured in exosome-depleted medium (complete medium depleted of FBS-derived exosomes by overnight centrifugation at  $100\,000 \times g$ ) for 48 h. Small EVs from culture supernatants were isolated by differential centrifugation at 300  $g$  for 10 min, 2 000  $\times g$  for 10 min, 10 000  $\times g$  for 30 min, and 100 000  $\times g$  for 70 min [31]. As EVs are not homogeneous [42], we used an EXOCEP exosome quantitation kit (System Biosciences Inc.) to quantitate the number of vesicles. Also, we used Exo-flow kits (System Biosciences Inc.) containing CD63 beads to show the purity of the EVs after high-speed centrifugation (Supplementary information, Figure S12). For osteogenesis assay, BMMSCs were pretreated with EVs (20  $\mu\text{g}/\text{ml}$ ) or PBS for 3 days and then cultured under osteoinductive conditions for 3 weeks, followed by Alizarin Red S staining.

#### Extracellular vesicle treatment in *Tsk*<sup>+</sup> mice

For *in vivo* EV tracking, PKH-26 (Sigma)-labeled EVs were intravenously infused into *Tsk*<sup>+</sup> mice. At 24 h post infusion, the femurs were fixed in 4% PFA and then decalcified with 5% EDTA, followed by optimal cutting temperature compound (OPT, Sakura Finetek, Torrance, CA, USA) embedding. Frozen sections were prepared, and slides were mounted with Vectashield mounting medium containing DAPI (Vector Laboratories, Burlingame, CA, USA). For *in vivo* treatments, EVs (100  $\mu\text{g}$ ) suspended in 200  $\mu\text{l}$  PBS or PBS (mock) were infused into *Tsk*<sup>+</sup> mice intravenously. Four weeks after the treatment, mice were killed for further analysis.

#### Ad-miR-151 treatment in *Tsk*<sup>+</sup> mice

miR-151 over-expressed Adenoviral-GFP vector (Ad-miR151, Applied Biological Materials Inc.) were amplified in HEK-293 cells, followed by purification and quantification using the Vir-aBind Adenovirus Miniprep Kit and QuickTiter Adenovirus Quantitation kit (Cell Biolabs Inc.) according to manufacturers' instruc-

tions. Ad-miR151 ( $2 \times 10^9$  p.f.u.) or empty vectors were injected into the *Tsk*<sup>+</sup> mice three times a week for up to 4 weeks. Samples will be harvested immediately after therapy for BMMSC isolation, histological assessments, and autoimmune index analysis. For *in vivo* exosome tracking, Ad-miR151 ( $2 \times 10^9$  p.f.u.) or an empty vector was injected into the *Tsk*<sup>+</sup> mice. At 24 h post infusion, the femurs were fixed in 4% PFA and then decalcified with 5% EDTA, followed by OPT embedding. Frozen sections were prepared, and slides were mounted with Vectashield mounting medium containing DAPI.

#### T-cell purification and differentiation

For *in vitro* polarization experiments, mouse CD4<sup>+</sup>CD62L<sup>+</sup> T lymphocytes were isolated from mouse total spleen cells using a magnetic sorting CD4<sup>+</sup>CD62L<sup>+</sup> T cell Isolation Kit II (Miltenyi Biotec, Auburn, CA, USA), according to the manufacturer's instructions. To activate T cells under T<sub>H</sub>0 condition, T cells were activated with plate-bound anti-CD3 and anti-CD28 (2 µg/ml each; BD Bioscience) in medium for 3 days. To activate T cells to T<sub>H</sub>2 condition, cells were activated for 72 h with plate-bound anti-CD3, anti-CD28, IL4 (20 ng/ml, R&D Systems), and anti-IFN $\gamma$  neutralizing antibodies (10 µg/ml, Biolegend).

#### Systemic sclerosis patients

This study was conducted in compliance with current Good Clinical Practice standards and in accordance with the principles set forth under the Declaration of Helsinki, 1989. The protocol (NCT00962923) was approved by the IRB of the Drum Tower Hospital of Nanjing University, Medical School, China. Informed consent was obtained from each patient.

#### Statistics

Comparisons between the two groups were analyzed using independent unpaired two-tailed Student's *t*-tests, and comparisons between more than two groups were analyzed using one-way ANOVA with the Bonferroni adjustment. *P*-values < 0.05 were considered statistically significant.

#### Acknowledgments

This work was supported by grants from National Institute of Dental and Craniofacial Research, National Institutes of Health, Department of Health and Human Services (R01DE017449 and R01DE019932 to SS and K99DE025915 to CC), an NIH NIAMS fellowship (T32AR007442), and an Schoenleber Pilot Research Grant from University of Pennsylvania School of Dental Medicine. Clinical studies were supported by grants from the China Major International (Regional) Joint Project (81120108021 to LS) and Jiangsu Province Major Research and Development Program (BE 2015062 to LS). ClinicalTrials.gov Identifier: NCT00962923.

#### Author Contributions

SS and LS conceived the project. SS, CC, and LS designed the experiments. CC, DW, AM, DL, XK, WY, and RY performed the experiments and analyzed the data. SS and CC wrote the manuscript.

#### Competing Financial Interests

The authors declare that they have no competing interests.

#### References

- Gabrielli A, Avvedimento EV, Krieg T. Mechanisms of disease scleroderma. *N Engl J Med* 2009; **360**:1989-2003.
- Omair MA, Pagnoux C, McDonald-Blumer H, Johnson SR. Low bone density in systemic sclerosis. A systematic review. *J Rheumatol* 2013; **40**:1881-1890.
- Atteritano M, Sorbara S, Bagnato G, *et al.* Bone mineral density, bone turnover markers and fractures in patients with systemic sclerosis: a case control study. *PLoS One* 2013; **8**:e66991.
- Kilic G, Kilic E, Akgul O, Ozgocmen S. Increased risk for bone loss in women with systemic sclerosis: a comparative study with rheumatoid arthritis. *Int J Rheum Dis* 2016; **19**:405-411.
- Mugino H, Ikemura K. Progressive systemic sclerosis with spontaneous fracture due to resorption of the mandible: a case report. *J Oral Maxillofac Surg* 2006; **64**:1137-1139.
- Auluck A, Pai KM, Shetty C, Sheno SD. Mandibular resorption in progressive systemic sclerosis: a report of three cases. *Dentomaxillofac Radiol* 2005; **34**:384-386.
- Souza RB, Borges CT, Takayama L, Aldrighi JM, Pereira RM. Systemic sclerosis and bone loss: the role of the disease and body composition. *Scand J Rheumatol* 2006; **35**:384-387.
- Barisic-Dujmovic T, Boban I, Adams DJ, Clark SH. Marfan-like skeletal phenotype in the tight skin (*Tsk*) mouse. *Calcif Tissue Int* 2007; **81**:305-315.
- Wynn TA. Fibrotic disease and the T(H)1/T(H)2 paradigm. *Nat Rev Immunol* 2004; **4**:583-594.
- Kodera T, McGaha TL, Phelps R, Paul WE, Bona CA. Disrupting the *IL-4* gene rescues mice homozygous for the tight-skin mutation from embryonic death and diminishes TGF- $\beta$  production by fibroblasts. *Proc Natl Acad Sci USA* 2002; **99**:3800-3805.
- Chen C, Akiyama K, Wang D, *et al.* IL4R $\alpha$ -mediated mTOR signaling determines mesenchymal stem cell lineage differentiation in fibrillin-1-mutant-induced osteopenia. *J Exp Med* 2014; **212**:73-91.
- Le Blanc K, Rasmusson I, Sundberg B, *et al.* Treatment of severe acute graft-versus-host disease with third party haploidentical mesenchymal stem cells. *Lancet* 2004; **363**:1439-1441.
- Sun L, Akiyama K, Zhang H, *et al.* Mesenchymal stem cell transplantation reverses multiorgan dysfunction in systemic lupus erythematosus mice and humans. *Stem Cells* 2009; **27**:1421-1432.
- Liang J, Gu F, Wang H, *et al.* Mesenchymal stem cell transplantation for diffuse alveolar hemorrhage in SLE. *Nat Rev Rheumatol* 2010; **6**:486-489.
- Liu X, Zheng P, Wang X, *et al.* A preliminary evaluation of efficacy and safety of Wharton's jelly mesenchymal stem cell transplantation in patients with type 2 diabetes mellitus. *Stem Cell Res Ther* 2014; **5**:57.
- Liang J, Li X, Zhang H, *et al.* Allogenic mesenchymal stem cells transplantation in patients with refractory RA. *Clin Rheumatol* 2012; **31**:157-161.
- Hatzistergos KE, Quevedo H, Oskouei BN, *et al.* Bone marrow mesenchymal stem cells stimulate cardiac stem cell proliferation and differentiation. *Circ Res* 2010; **107**:913-922.

- 18 Sakaida I, Terai S, Yamamoto N, *et al.* Transplantation of bone marrow cells reduces CCl<sub>4</sub>-induced liver fibrosis in mice. *Hepatology* 2004; **40**:1304-1311.
- 19 Yamada Y, Ueda M, Hibi H, Baba S. A novel approach to periodontal tissue regeneration with mesenchymal stem cells and platelet-rich plasma using tissue engineering technology: a clinical case report. *Int J Periodontics Restorative Dent* 2006; **26**:363-369.
- 20 Kishk NA, Gabr H, Hamdy S, *et al.* Case control series of intrathecal autologous bone marrow mesenchymal stem cell therapy for chronic spinal cord injury. *Neurorehabil Neural Repair* 2010; **24**:702-708.
- 21 Liu J, Han D, Wang Z, *et al.* Clinical analysis of the treatment of spinal cord injury with umbilical cord mesenchymal stem cells. *Cytotherapy* 2013; **15**:185-191.
- 22 Chen X, Armstrong MA, Li G. Mesenchymal stem cells in immunoregulation. *Immunol Cell Biol* 2006; **84**:413-421.
- 23 Scuderi N, Ceccarelli S, Onesti MG, *et al.* Human adipose-derived stem cells for cell-based therapies in the treatment of systemic sclerosis. *Cell Transplant* 2013; **22**:779-795.
- 24 Ren G, Zhang L, Zhao X, *et al.* Mesenchymal stem cell-mediated immunosuppression occurs via concerted action of chemokines and nitric oxide. *Cell Stem Cell* 2008; **2**:141-150.
- 25 Choi H, Lee RH, Bazhanov N, Oh JY, Prockop DJ. Anti-inflammatory protein TSG-6 secreted by activated MSCs attenuates zymosan-induced mouse peritonitis by decreasing TLR2/NF-kappaB signaling in resident macrophages. *Blood* 2011; **118**:330-338.
- 26 Meisel R, Zibert A, Laryea M, Gobel U, Daubeber W, Dilloo D. Human bone marrow stromal cells inhibit allogeneic T-cell responses by indoleamine 2,3-dioxygenase-mediated tryptophan degradation. *Blood* 2004; **103**:4619-4621.
- 27 Nemeth K, Leelahavanichkul A, Yuen PS, *et al.* Bone marrow stromal cells attenuate sepsis via prostaglandin E(2)-dependent reprogramming of host macrophages to increase their interleukin-10 production. *Nat Med* 2009; **15**:42-49.
- 28 Akiyama K, Chen C, Wang D, *et al.* Mesenchymal-stem-cell-induced immunoregulation involves FAS-ligand-/FAS-mediated T cell apoptosis. *Cell Stem Cell* 2012; **10**:544-555.
- 29 Chen C, Akiyama K, Yamaza T, *et al.* Telomerase governs immunomodulatory properties of mesenchymal stem cells by regulating FAS ligand expression. *EMBO Mol Med* 2014; **6**:322-334.
- 30 Hayes J, Peruzzi PP, Lawler S. MicroRNAs in cancer: biomarkers, functions and therapy. *Trends Mol Med* 2014; **20**:460-469.
- 31 They C, Amigorena S, Raposo G, Clayton A. Isolation and characterization of exosomes from cell culture supernatants and biological fluids. *Curr Protoc Cell Biol* 2006; **Chapter 3**:Unit3.22.
- 32 Dreux M, Garaigorta U, Boyd B, *et al.* Short-range exosomal transfer of viral RNA from infected cells to plasmacytoid dendritic cells triggers innate immunity. *Cell Host Microbe* 2012; **12**:558-570.
- 33 Li J, Liu K, Liu Y, *et al.* Exosomes mediate the cell-to cell transmission of IFN- $\alpha$ -induced antiviral activity. *Nat Immunol* 2013; **14**:793-803.
- 34 Luga V, Zhang L, Vitoria-Petit AM, *et al.* Exosomes mediate stromal mobilization of autocrine Wnt-PCP signaling in breast cancer cell migration. *Cell* 2012; **151**:1542-1556.
- 35 Boelens MC, Wu TJ, Nabet BY, *et al.* Exosome transfer from stromal to breast cancer cells regulates therapy resistance pathways. *Cell* 2014; **159**:499-513.
- 36 Liu S, Liu D, Chen C, *et al.* MSC transplantation improves osteopenia via epigenetic regulation of Notch signaling in lupus. *Cell Metab* 2015; **22**:606-618.
- 37 Liu Y, Wang L, Liu S, *et al.* Transplantation of SHED prevents bone loss in the early phase of ovariectomy-induced osteoporosis. *J Dent Res* 2014; **93**:1124-32.
- 38 Ono M, Kosaka N, Tominaga N, *et al.* Exosomes from bone marrow mesenchymal stem cells contain a microRNA that promotes dormancy in metastatic breast cancer cells. *Sci Signal* 2014; **7**:ra63.
- 39 Baglio SR, Rooijers K, Koppers-Lalic D, *et al.* Human bone marrow- and adipose-mesenchymal stem cells secrete exosomes enriched in distinctive miRNA and tRNA species. *Stem Cell Res Ther* 2015; **6**:127.
- 40 Wang B, Yao K, Huuskens BM, *et al.* Mesenchymal stem cells deliver exogenous microRNA-let7c via exosomes to attenuate renal fibrosis. *Mol Ther* 2016; **24**:1290-1301.
- 41 Soifer HS, Rossi JJ, Saetrom P. MicroRNAs in disease and potential therapeutic applications. *Mol Ther* 2007; **15**:2070-2079.
- 42 Witwer KW, Buzas EI, Bemis LT, *et al.* Standardization of sample collection, isolation and analysis methods in extracellular vesicle research. *J Extracell Vesicles* 2013; **2**:jev.v2i0.20360.
- 43 Ostrowski M, Carmo NB, Krumeich S, *et al.* Rab27a and Rab27b control different steps of the exosome secretion pathway. *Nat Cell Biol* 2010; **12**:19-30.
- 44 Nauta AJ, Fibbe WE. Immunomodulatory properties of mesenchymal stem cells. *Blood* 2007; **110**:3499-3506.
- 45 Uccelli A, Moretta L, Pistoia V. Mesenchymal stem cells in health and disease. *Nat Rev Immunol* 2008; **8**:726-736.
- 46 Bernardo ME, Locatelli F, Fibbe WE. Mesenchymal stromal cells. *Ann NY Acad Sci* 2009; **1176**:101-117.
- 47 Maria AT, Toupet K, Bony C, *et al.* Antifibrotic, Antioxidant, and immunomodulatory effects of mesenchymal stem cells in HOCl-induced systemic sclerosis. *Arthritis Rheumatol* 2016; **68**:1013-1025.
- 48 Maria AT, Toupet K, Maumus M, *et al.* Human adipose mesenchymal stem cells as potent anti-fibrosis for systemic sclerosis. *J Autoimmun* 2016; **70**:31-39.
- 49 Wang D, Feng X, Lu L, *et al.* A CD8 T cell/indoleamine 2,3-dioxygenase axis is required for mesenchymal stem cell suppression of human systemic lupus erythematosus. *Arthritis Rheumatol* 2014; **66**:2234-2245.
- 50 Golpanian S, Wolf A, Hatzistergos KE, Hare JM. Rebuilding the damaged heart: mesenchymal stem cells, cell-based therapy, and engineered heart tissue. *Physiol Rev* 2016; **96**:1127-1168.
- 51 Mastro-Martinez I, Perez-Suarez E, Melen G, *et al.* Effects of local administration of allogenic adipose tissue-derived mesenchymal stem cells on functional recovery in experimental traumatic brain injury. *Brain Inj* 2015; **29**:1497-1510.
- 52 Montecalvo A, Larregina AT, Shufesky WJ, *et al.* Mechanism of transfer of functional microRNAs between mouse dendritic

- cells via exosomes. *Blood* 2012; **119**:756-766.
- 53 Xin H, Li Y, Cui Y, Yang JJ, Zhang ZG, Chopp M. Systemic administration of exosomes released from mesenchymal stromal cells promote functional recovery and neurovascular plasticity after stroke in rats. *J Cereb Blood Flow Metab* 2013; **33**:1711-1715.
- 54 Li T, Yan Y, Wang B, *et al.* Exosomes derived from human umbilical cord mesenchymal stem cells alleviate liver fibrosis. *Stem Cell Dev* 2013; **15**:845-854.
- 55 Lai RC, Chen TS, Lim SK. Mesenchymal stem cell exosome: a novel stem cell therapy for cardiovascular disease. *Regen Med* 2011; **6**:481-492.
- 56 Yeo RW, Lai RC, Zhang B, *et al.* Mesenchymal stem cell: an efficient mass producer of exosomes for drug delivery. *Adv Drug Deliv Rev* 2013; **65**:336-341.
- 57 Ciechomska M, van Laar JM, O'Reilly S. Emerging role of epigenetics in systemic sclerosis pathogenesis. *Genes Immun* 2014; **15**:433-439.
- 58 Jimenes SA, Piera-Velazquez S. Potential role of human-specific genes, human-specific microRNAs and human-specific non-coding regulatory RNAs in the pathogenesis of systemic sclerosis and Sjogern's syndrome. *Autoimmun Rev* 2013; **12**:1046-1051.
- 59 Li Y, Huang J, Guo M, Zuo X. MicroRNAs regulating signaling pathways: potential biomarkers in systemic sclerosis. *Genomics Proteomics Bioinformatics* 2015; **13**:234-241.
- 60 Clark EA, Kalomoiris S, Nolta JA, Fierro FA. Concise review: microRNA function in multipotent mesenchymal stem cells. *Stem Cells* 2014; **32**:1074-1082.
- 61 Li CJ, Cheng P, Liang MK, *et al.* MicroRNA-188 regulates age-related switch between osteoblast and adipocyte differentiation. *J Clin Invest* 2015; **125**:1509-1522.
- 62 Broderick JA, Zamore PD. MicroRNA therapeutics. *Gene Therapy* 2011; **18**:1104-1110.
- 63 Bonci D, Coppola V, Musumeci M, *et al.* The mi-R15a-miR16-1 cluster controls prostate cancer by targeting multiple oncogenic activities. *Nat Med* 2008; **14**:1271-7.
- 64 Zhu H, Guo ZK, Jiang XX, *et al.* A protocol for isolation and culture of mesenchymal stem cells from mouse compact bone. *Nat Protoc* 2010; **5**:550-560.
- 65 Soleimani M, Nadri S. A protocol for isolation and culture of mesenchymal stem cells from mouse bone marrow. *Nat Protoc* 2009; **4**:102-106.
- 66 Miura M, Miura Y, Padilla-Nash HM, *et al.* Accumulated chromosomal instability in murine bone marrow mesenchymal stem cells leads to malignant transformation. *Stem Cells* 2006; **24**:1095-1103.
- 67 Boregowda SV, Krishnappa V, Chambers JW, *et al.* Atmospheric oxygen inhibits growth and differentiation of marrow-derived mouse mesenchymal stem cells via a p53-dependent mechanism: implications for long-term culture expansion. *Stem Cells* 2012; **30**:975-987.
- 68 Phinney DG. Functional heterogeneity of mesenchymal stem cells: implications for cell therapy. *J Cell Biochem* 2012; **113**:2806-2812.

(Supplementary information is linked to the online version of the paper on the *Cell Research* website.)